

# Low-dimensional wide-bandgap semiconductors for UV photodetectors

Ziqing Li<sup>1,3</sup>, Tingting Yan<sup>2,3</sup> & Xiaosheng Fang<sup>1,2</sup>✉

## Abstract

Accurate UV light detection is a crucial component in modern optoelectronic technologies. Current UV photodetectors are mainly based on wide-bandgap semiconductors (WBSs), such as III–V semiconductors. However, conventional WBSs have reached a bottleneck of low integration and inflexibility. In this regard, low-dimensional WBSs, which have suitable UV absorption, tunable performance and good compatibility, are appealing for diversified UV applications. UV photodetectors based on low-dimensional WBSs have broad application prospects in imaging, communication, multispectral and/or weak light detection and flexible and wearable electronics. This Review focuses on the progress, open challenges and outlook in the field of UV photodetectors on the basis of low-dimensional WBSs. We examine how material design, dimensionality engineering and device engineering of WBSs can control their morphological structures and properties and attempt to clarify the interplay among material growth, device structure and application scenarios.

## Sections

Introduction

Common WBS UV photodetectors

Dimensionality engineering and tunable performance

Device design

Applications

Challenges and outlook

<sup>1</sup>Shanghai Frontiers Science Research Base of Intelligent Optoelectronics and Perception, Institute of Optoelectronics, Fudan University, Shanghai, P. R. China. <sup>2</sup>Department of Materials Science, State Key Laboratory of Molecular Engineering of Polymers, Fudan University, Shanghai, P. R. China. <sup>3</sup>These authors contributed equally: Ziqing Li, Tingting Yan. ✉e-mail: [xshfang@fudan.edu.cn](mailto:xshfang@fudan.edu.cn)

## Introduction

### UV photodetector industry

UV research began as early as the nineteenth century, focusing on invisible radiation beyond blue light<sup>1</sup>. UV radiation is divided into three main spectral regions: UVC (200–280 nm) radiation, which is completely absorbed by the ozone layer and cannot reach the ground, and thus there is little background radiation of this region on the surface of the Earth; UVB (280–320 nm) radiation, most of which is absorbed by the atmosphere, but the 2% that reaches the surface of the Earth can be harmful to the human body and cause skin diseases; and UVA (320–400 nm) radiation, which can penetrate atmospheric clouds to reach the ground and can cause skin damage and wrinkles in large doses. The deep-UV region generally refers to radiation <280 nm. UV radiation <200 nm, called vacuum UV (10–200 nm), is easily absorbed by molecules and cannot propagate in the air. The effects of UV radiation on organisms and materials will vary greatly depending on its specific wavelengths. However, because UV radiation cannot be observed by the naked eye, UV technology has been developed rapidly to observe and quantify it, including UV spectroscopy<sup>2</sup>, UV light sources<sup>3</sup> and UV sensors<sup>4</sup>.

UV sensors, which include photochromic sensors and photodetectors, are devices that detect and measure levels of UV radiation. Photochromic sensors have poor repeatability and low instantaneous response intensity and cannot detect weak light<sup>5,6</sup>. UV photodetectors, which convert UV light signals into electrical signals, are utilized to detect the UV radiation level and are considered to be crucial components of modern optoelectronic technologies<sup>7</sup>. Compared with infrared (IR) photodetection, UV photodetection is not susceptible to long-wavelength electromagnetic interference, and it has a good concealment. UV photodetection is an indispensable key component in civil fields, scientific research and military fields<sup>3,8</sup>. In daily life, accurate detection of UV radiation intensity and dose are required in sterilization, water purification, environmental monitoring and UV curing technologies. In scientific research, UV photodetection is widely used in medicine and biology, because UV light is easily absorbed by biomolecules and is only slightly interfered with by background signals; it also has important applications in space detection. In military defence, solar-blind and visible-blind UV photodetectors have unique advantages in UV communication, detection and warning. The transmission distance of UV communication can be up to a few kilometres, and it is also able to bypass obstacles by reflection and scattering processes. In addition, solar-blind radiation is nearly absorbed by oxygen and ozone in the atmosphere and thus demonstrates a low background noise near the ground<sup>9</sup>. These unique features make UV communication especially attractive for secure communication and military communication. For example, a UV communication system consisting of an Si-based avalanche photodiode showed a record data rate as high as 2.4 Gb s<sup>-1</sup> (ref. 9).

With the growing popularity of sensing technology, the broad UV photodetector market covers diverse consumer electronics and industry applications (Fig. 1a), such as automotive, pharmaceutical, medical diagnostics, environmental monitoring and industrial process control, among others<sup>3,9–14</sup>. The consumer electronics segment has a great demand for UV photodetectors, which serve as disinfecting devices in fabricating smartphones, tablets, watches, laptops and video game controllers. The up-to-date global market of UV photodetectors is boosted by rising investment in the smartphone segment and elevated efficiency of the automotive market<sup>15</sup>. The UV disinfection industry has risen in popularity given increasing demands from biopharma

and pharmaceuticals, especially during the COVID-19 pandemic, in which UV photodetectors are used to monitor the level of UVC radiation across laboratory environments during sterilization<sup>13</sup>, and from water treatment plants, in which UV disinfection systems kill bacteria and viruses. UV photodetectors are also used to detect the presence of seals, labels, pills and other packing items in the packaging industry and to monitor fermentation tanks in global industrial processes in which bacteria are completely removed from liquids. UVA/B sensors are primarily used in our daily lives<sup>14</sup>. UVA sensors have the ability to sensitively and accurately detect objects in dark areas, which is useful in numerous applications such as electronic toll collection systems and automotive security systems. The main UVB sensor applications include clinical trial, food safety and air quality monitoring.

Because the market size of UV photodetectors is greatly increasing with demand for photodetection chips, searching for and optimizing UV-sensitive semiconductors is at the core of UV photodetector development. Commercial UV photodetectors have mainly been Si-based UV photodiodes and UV photomultiplier tubes<sup>16</sup>. UV photomultiplier tubes are capable of high-response UV photodetection, but their practical application is limited by requiring low-temperature working conditions and high power supply (above 1-kV voltage)<sup>16</sup>. Although Si-based UV photodiodes show a broad response range from the UV to near-IR regions, their low responsivity in the UV wavelength ranges and the requirement of optical filter systems limits their UV photodetection application. The third-generation wide-bandgap semiconductors (WBSs) represented by GaN, SiC, Ga<sub>2</sub>O<sub>3</sub>, ZnO and diamond, among others, have been emerging as potential alternatives for constructing filterless UV photodetectors, owing to their suitable cut-off wavelength within the UV wavelength<sup>7</sup>.

WBSs themselves have chemical stability, good thermal conductivity and high saturation electron drift speed, making them ideal semiconducting materials for fabricating UV photodetectors. Compared with the early UV photomultiplier tubes and Si-based UV photodiodes, UV photodetectors based on WBSs have the advantages of low operating voltage, low noise and high sensitivity<sup>16</sup>. WBS-based UV photodetectors can also selectively detect UVA, UVB or UVC wavelengths and distinguish their UV composition. Among these photodetectors, the research development and industrial application of those based on GaN and SiC materials are relatively mature, and their products include photodetection probes, spectrometers, photodetection chips and other UV modules. With technological advancements making UV photodetectors more affordable and efficient, their current global market is expected to grow ever broader in various applications. Thus, it is necessary to develop more WBSs and design new structures to satisfy the increasing requirements for diversified UV applications.

### Low-dimensional wide-bandgap semiconductors for UV photodetectors

Great progress in high-performance photodetection has been made in group III-nitrides (BN, AlN, GaN and InN)<sup>17,18</sup>. Although inch-size wafers can be successfully grown, integrated photodetectors still encounter serious current interference. Moreover, as UV light penetrates at a shallower depth than visible and IR light, reducing the length scale of the material down to UV penetration depths can substantially decrease visible and IR absorption and also potentially supply mechanical flexibility lacking in the bulk<sup>19</sup>. In this regard, patterned low-dimensional structures (herein referring to 0D, 1D and 2D nanomaterials) of WBSs can be suitable for highly integrated and efficient photodetectors.

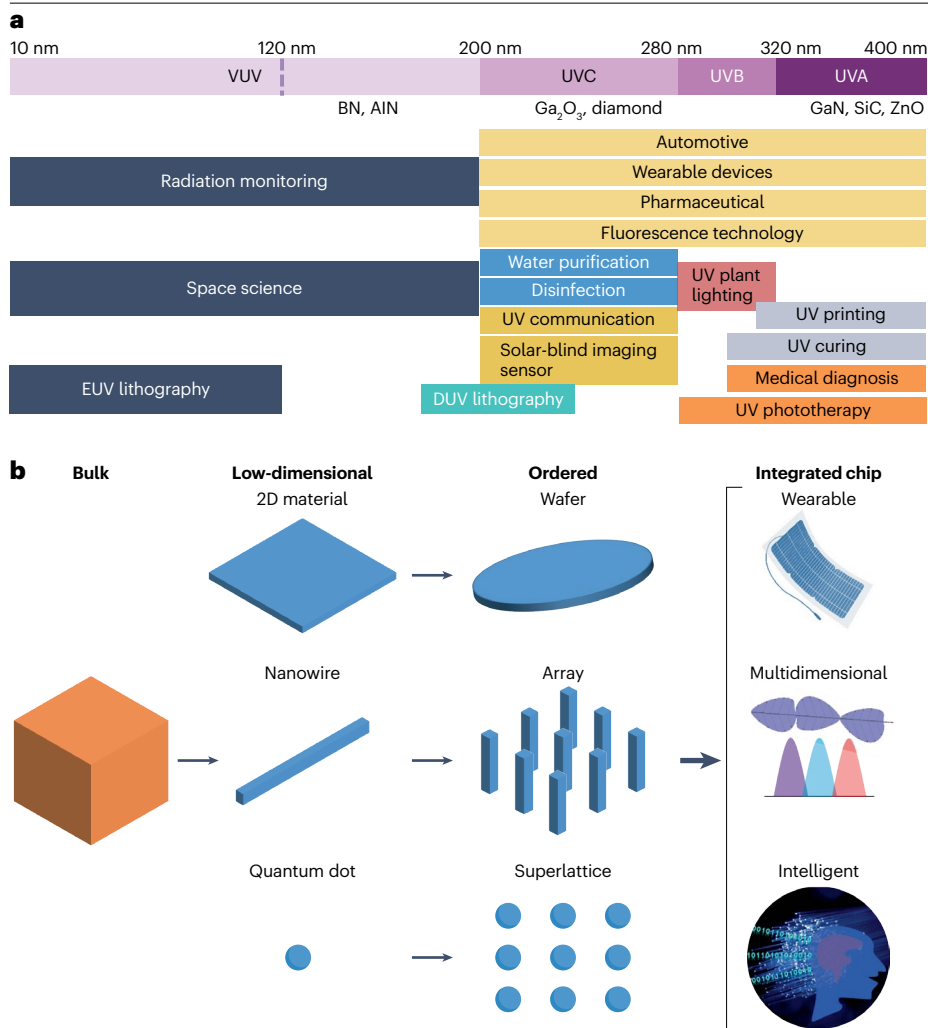


**Fig. 1 | Applications and development of UV photodetectors.** **a**, Various industry, life and military applications exist for the UVA, UVB, UVC, vacuum UV (VUV) and extreme UV (EUV) spectral regions, such as consumer electronics, automotive, pharmaceutical, medical diagnostics, environmental monitoring and industrial process control<sup>3,9–14</sup>. **b**, By substantially reducing length scale, bulk wide-bandgap semiconductors are developed into low-dimensional nanomaterials (2D materials, 1D nanowires and 0D quantum dots) that exhibit flexibility and distinctive electronic structure. These low-dimensional nanomaterials can be further assembled into large-area ordered materials, such as wafer-scale thin layers, nanowire arrays and quantum dot superlattices. Finally, integrated chips are fabricated featuring wearable, intelligent and multidimensional functions, the latter of which includes acquiring multidimensional information of wavelength, polarization, phase and optical path. BN, boron nitride; DUV, deep UV.

From the view of electronic structure, when a WBS forms a low-dimensional structure, its quasi-continuous band structure will split into discrete quantum energy levels, and the absorbed photon energy is obviously different from the bulk structure. In various low-dimensional structures, 2D quantum structures easily form a 2D electron or hole gas, which is more conducive to current transport<sup>20</sup>. The discrete quantum energy levels of low-dimensional semiconductors enable ultra-narrowband photodetectors. Moreover, wide-bandgap 2D materials that are only a few atomic layers thick make flexible UV photodetectors possible<sup>21</sup>, such as those based on wafer-scale few-layered BN, ultrathin 2D GaN single crystal and chip-less GaN.

Following these lines of thought, bulk WBSs have been developed into low-dimensional nanomaterials (typically 2D materials<sup>21</sup>, 1D nanowires<sup>22</sup> or 0D quantum dots<sup>23</sup>) that exhibit flexibility and distinctive electronic structure (Fig. 1b). These materials can be further assembled into large-area ordered materials, such as wafer-scale ultrathin layers, nanowire arrays and quantum dot superlattices. Finally, integrated chips featuring wearable, multidimensional and intelligent functions are fabricated.

This Review focuses on the tunable properties of low-dimensional WBSs and their application potential in next-generation UV photodetectors. We outline how specific properties of low-dimensional WBSs are regulated by different technical routes, providing a roadmap for designing novel UV-sensitive semiconductors. We also examine diverse applications and the challenges that must be met to satisfy their requirements in complex scenarios. The Review aims to motivate more researchers to work on structure design, material synthesis and functional application of UV detection technology.

## Common WBS UV photodetectors Classification and working mechanisms

Two-terminal photodetectors can be classified as photoconductor, Schottky, metal–semiconductor–metal, PN junction, PIN junction and avalanche photodiode types<sup>24</sup>. Both electrode–semiconductor interfaces should have ohmic contact in photoconductor, PN junction and PIN junction photodetectors. The photoconductor usually displays high current gain and slow photoresponse speed, whereas PN or PIN junctions show fast photoresponse owing to the large built-in electrical field. In Schottky and avalanche architectures,

one electrode–semiconductor interface should have ohmic contact, and the other should have Schottky contact<sup>24,25</sup>. To this point, the optoelectronic performance of Schottky photodetectors is greatly affected by the high Schottky barrier. Under the combined influence of Schottky and junction barriers, the avalanche photodetector can exhibit ultrahigh current gain and ultrafast photoresponse speed, even for detecting ultraweak light<sup>26</sup>. Finally, both electrode interfaces of the metal–semiconductor–metal structure are Schottky contacts. A typical three-terminal photodetector is called a phototransistor, which exhibits suppressed noise and amplifying photocurrent<sup>8</sup>.

## Preparation routes

**2D nanomaterial wafers.** Wide-bandgap 2D semiconductors can be prepared by universal top-down (such as liquid metal printing technique, mechanical exfoliation and ion-exchange exfoliation) and bottom-up (such as chemical vapour deposition, molecular beam epitaxy and wet-chemical synthesis) growth methods<sup>27</sup>. The nucleation and growth of bottom-up methods involve the transition metal-catalysed dissociation of feedstocks, the diffusion templates of the decomposed precursor and their self-assembly into thick islands. However, these methods fail to fabricate large-area ordered single-crystalline thin films.

In an example of a bottom-up method, a wafer-scale single-crystalline hexagonal boron nitride (h-BN) film was grown through self-collimated grain formation<sup>28</sup>. There is an individual minimum in the formation energy profile of h-BN grain boundaries, in which the configuration is more stable than other orientations<sup>29</sup> (Fig. 2a). Thus, the h-BN islands rotate and align on the liquid Au surface to this minimum-energy orientation. These ordered grains then seamlessly coalesce to produce the wafer-scale single-crystalline h-BN films. This self-collimated grain formation method is a universal strategy to prepare free-standing ultrathin wide-bandgap 2D semiconductor wafers.

Inspired by the vicinal step growth, a 100-cm<sup>2</sup> single-crystalline h-BN thin film was epitaxially fabricated on a copper substrate<sup>30</sup>. The formation energy of h-BN along Cu <211> theoretically shows an energy minimum at  $\gamma = 0^\circ$  on the Cu(110) substrate, in which  $\gamma$  is the angle between the h-BN zigzag and Cu <211> step (Fig. 2b). The meandering step edge includes the straight step edge segment and adjacent segments between the atomic kinks, thus the complementary kinks ensure the growth of unidirectionally aligned 2D islands along winding step edges on substrates<sup>31,32</sup>. This growth principle is universal in that inversion symmetry breaking is used in the epitaxial preparation of single-crystalline h-BN, which can be generalized to large-area single crystals of other wide-bandgap 2D materials.

Remote epitaxy through graphene, which enables the growth, release and transfer of large-area 2D materials, was able to realize a free-standing single-crystalline layer and free transfer<sup>33</sup>. In the typical process of remote epitaxy, the adopted 2D van der Waals (vdW) material serves as a semi-transparent interlayer to enable remote epitaxial growth and the release of target 2D materials (Fig. 2c). The monolayered 2D interlayer cannot completely screen the electrostatic potential of the substrate, and the adatoms on the 2D interlayer can still interact with the substrate lattice, thus leading to remote epitaxy between adatoms and substrate lattices. This method allows epitaxy on 2D materials induced by weak vdW interactions, which opens the door for fabricating highly ordered ultrathin WBSs<sup>34,35</sup>.

**1D nanomaterial arrays.** One of the most common top-down methods to produce nanowires is using a mask and dry etching, directly

making nanometre dimensions and subsequently smoothing the rough surface<sup>22,36</sup>. To provide better control over the nanowire quality, bottom-up seeded growth from metal nanoparticles can also be a good choice. Au and Ni nanoparticles and their alloys are widely used as the metal seeds for the growth of GaN nanowires. The orientation of the as-grown nanowires is determined by the substrate type (sapphire substrate, LiAlO<sub>2</sub>, silicon wafer and so on), the growth conditions (temperature, atmosphere and so on) and the characteristics of the interface between the metal nanoparticles and GaN<sup>37,38</sup>. This method easily obtains <11–20> or <10–10> oriented nanowires, but it is difficult to obtain <0001> oriented nanowires on sapphire<sup>39</sup>.

Self-organized growth (such as self-seeded growth) is another growth method, in which molecular beam epitaxy is usually used to control the nucleation and growth process of GaN nanowires. The growth parameters include Ga flux, substrate morphology and substrate temperature, among others<sup>40</sup>. This method can effectively achieve substrate-independent growth of <0001> oriented nanowires, whereas the material polarity (Ga-polar or N-polar) cannot be well controlled. Additionally, n-type or p-type GaN can be obtained by doping with Si, Mg or Ge, but the spatial homogeneity of the dopant content is insufficient<sup>41</sup>.

Template-assisted selective-area growth is an effective method for preparing large-area, vertically aligned and uniform nanowire arrays (Fig. 2d). Regulating the size, depth and number of mask holes can tailor the ordered arrays of patterned nanowires. At continuous-flow mode, a pyramid shape forms at the hole, and the continued growth forms a new crystal surface between the pyramid cap and the bottom. The side facets stop lateral growth, limiting the diameter of the nanowires, whereas the continued growth of the pyramid surface continues to increase the nanowire length<sup>42</sup>.

**OD nanomaterial superlattices.** WBS quantum dot superlattices, which can be assembled by slow evaporation of solvents from colloidal dispersions, are currently in their infancy<sup>15</sup>. Some notable progress has been made in PbSe colloidal quantum dot superlattices, such as shape control, oriented self-assembly<sup>43</sup> and high mobility<sup>43–45</sup>. This considerable mobility is ascribed to the electron coupling interaction in the highly ordered superlattices. It is believed that quantum dot superlattices of WBSs can be fabricated in the near future by adjusting the energy levels, interparticle coupling and structural arrangement of the quantum dots<sup>46,47</sup>.

## Dimensionality engineering and tunable performance

Basic optoelectronic performance metrics of a photodetector, including responsivity ( $R_s$ ), specific detectivity ( $D^*$ ), response speed and external quantum efficiency (EQE), are summarized in Table 1 and Box 1. These metrics form a comprehensive evaluation of a photodetector.

To date, OD, 1D and 2D nanomaterials are all capable of relatively high UV photodetection, although detection of deep-UV light suffers from a low responsivity<sup>48,49</sup> (Fig. 3a). Fast response speed can be realized in 1D and 2D nanomaterials, especially ordered structures such as nanowire arrays and single-crystalline 2D materials. However, OD material-based photodetectors suffer from slow response speed; the decay time of some devices may last for tens or hundreds of seconds. Much effort has been paid to improving photodetector decay speed, especially in OD material-based systems<sup>50</sup> (Fig. 3b). In this section, we focus on working processes of a photodetector (photon absorption, charge separation, carrier transport and carrier collection) to outline



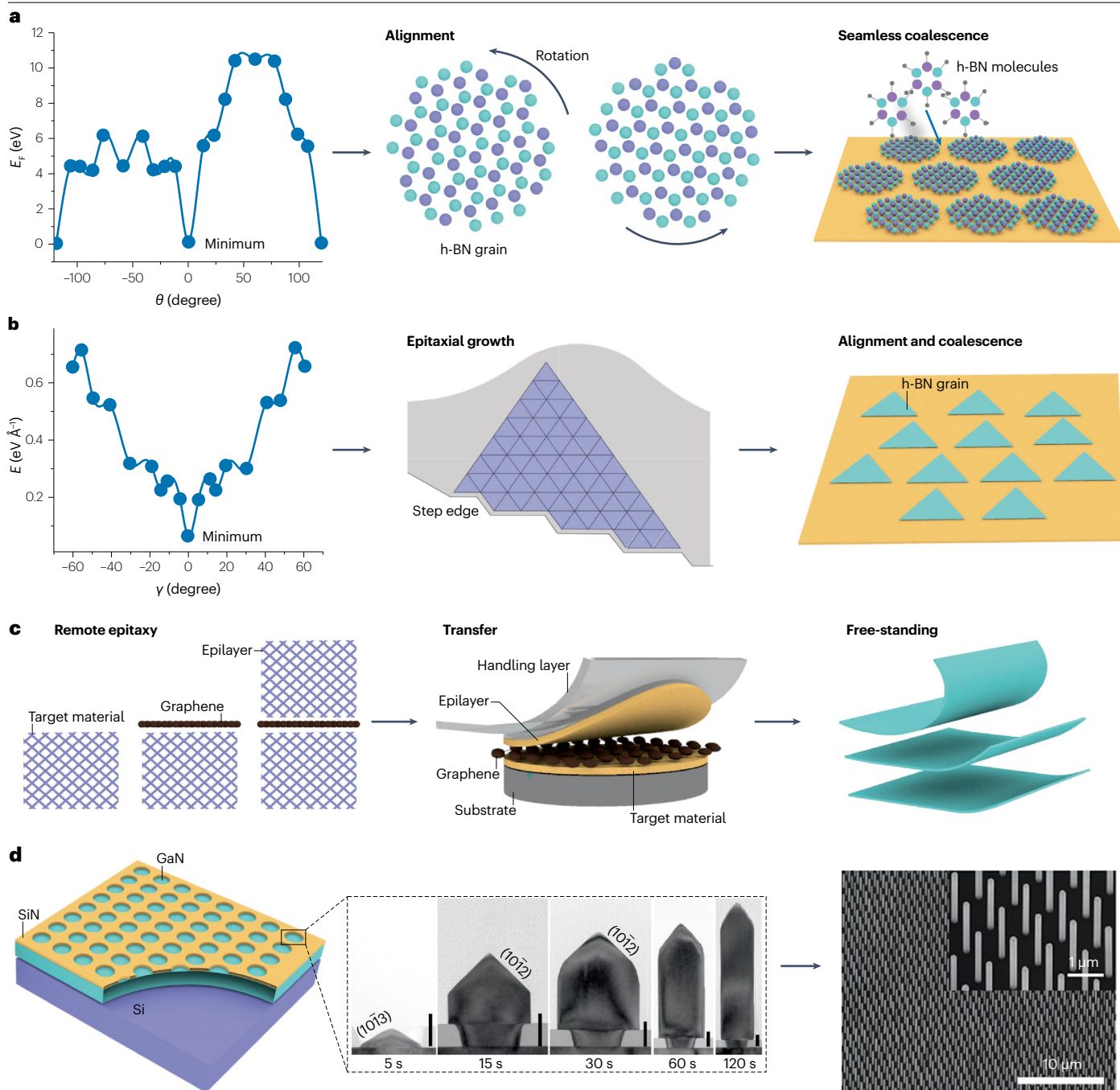


**Fig. 2 | Ordered assembly of large-area single-crystalline low-dimensional wide-bandgap semiconductors and their basic mechanisms. a**, Self-collimated grain formation of hexagonal boron nitride (h-BN) single-crystalline thin film. The formation energy minimum represents the most stable in-plane orientation of the h-BN grain. The growth process includes grain rotation, alignment and seamless coalescence<sup>28,29</sup>. **b**, Epitaxial growth of h-BN single-crystalline thin film on copper. The formation energy minimum represents the most stable epitaxial direction along the vicinal step. Growth is activated by the step edge and results in unidirectionally aligned grains<sup>30,32</sup>. **c**, Remote epitaxy adopts a 2D van der Waals material as an interlayer to grow a free-standing, single-crystalline

thin film, including numerous wide-bandgap semiconductors<sup>34</sup>. **d**, Selective area epitaxial growth of GaN nanowire arrays. A mask is patterned with nanometre-sized circular openings, inside which pyramid facets develop to form new facets at the edges between the vertical side facets and the top pyramid, and finally grow into nanowires in the continuous-flow mode<sup>18</sup>. Panel **a** adapted with permission from ref. 28, AAAS, and ref. 29, APS. Panel **b** adapted from ref. 30, Springer Nature Limited, and adapted with permission from ref. 32, copyright 2019 American Chemical Society. Panel **d** reprinted with permission from ref. 18, copyright 2019 American Chemical Society.

**Table 1 | Performance parameters and definitions of photodetectors**

Metric	Unit	Definition
Photocurrent ( $I_{ph}$ )	A	Generated current stimulated by illumination
Dark current ( $I_d$ )	A	Current in dark state
On-off ratio	–	Ratio of photocurrent to dark current
Gain (G)	–	Number of detected carriers divided by number of absorbed photons
Responsivity ( $R_\lambda$ )	A W <sup>-1</sup>	Photocurrent at a certain wavelength divided by incident light power
External quantum efficiency (EQE)	%	Ratio of the number of collected electrons to the number of incident photons
Specific detectivity ( $D^*$ )	cm Hz <sup>1/2</sup> W <sup>-1</sup> (Jones)	Spectral detection rate per unit surface area (1 cm <sup>2</sup> ) and per unit bandwidth (1 Hz)
Response time (t)	s	Rise time ( $t_r$ ) is the period from 10% to 90% of the maximum photocurrent. Decay time ( $t_d$ ) is the period from 90% to 10% of the maximum photocurrent
–3 dB bandwidth (BW)	Hz	Modulation frequency of responsivity of the photodetector is half of that at steady state
Noise current ( $I_N$ )	A	Root mean square of current fluctuation
Noise-equivalent power (NEP)	W	Optical power required to generate the given noise current spectral density
Linear dynamic range	dB	Range of incident light power for linear response

the optoelectronic performance development of photodetectors based on low-dimensional WBSs, as shown in Table 2. The relationship between low-dimensional structure and tunable performance is discussed in detail.

## 0D nanomaterials

In 0D semiconductors, charge carriers (holes and electrons) are constrained inside the nanoparticles or quantum dots, limiting carrier transport in three dimensions. This constraint leads to a poor photodetecting performance with low responsivity and slow response speed. Nanoparticles are difficult to assemble into dense films, so they will cause large current leakage in vertical photodiode structures; thus, photodetectors based on nanoparticle semiconductors commonly use horizontal photoconductor structures<sup>51</sup>. Ordered quantum dot superlattices can be an effective route to enhance the carrier mobility and thus improve the optoelectronic performance<sup>44,45</sup>.

0D nanoparticles have the advantage of being compatible with other semiconductor chips through solution-processed methods (spin coating, spray coating, injecting, scraping and so on). Commercially available silicon wafers, which have long been applied for detecting broadband light, are taken as an example. Owing to the shallow penetration depth (to high-frequency photons), high reflection coefficient and hot electron loss, Si displays a low responsivity to UV light<sup>52,53</sup>. 0D wide-bandgap ZnMgO quantum dots, given their excellent UV photodetecting ability, were easily spin-coated on Si chips to make up for the shortcomings of the latter in the UV region<sup>54</sup>. Meanwhile, because these quantum dots are almost transparent in the visible and IR regions, and the thickness of the layer of nanoparticles can be easily regulated to minimize the light loss attributed to wave-guiding effects or internal reflection, they will not deteriorate the performance of the photodetector in the visible–IR region (Fig. 3c).

Oxide semiconductor nanoparticles have seen great development in the UV detection field. Owing to the large surface-to-volume ratio in nanoparticles, many oxygen vacancies are produced in these oxide particles, resulting in a high conductivity and responsivity; however, these vacancies may act as dense surface trapping states to capture free electrons, impeding the adsorption and desorption of oxygen molecules and thus greatly slowing down the response speed of the

photodetector<sup>50,55</sup>. To improve the response speed, the surface of the 0D semiconductors can be modified with inorganic, organic, metallic or other non-semiconductor types of nanoparticles<sup>56–58</sup>. For example, graphdiyne nanoparticles were assembled electrostatically onto the surface of ZnO nanoparticles to form graphdiyne:ZnO nanocomposites<sup>59</sup>. Interfaces between the two nanoparticle types create abundant PN junctions throughout the whole film and can expand the depletion regions for the photodetector to rapidly dissipate the photo-induced current as light switches off (Fig. 3d). In addition, the minority carriers become trapped in the introduced heterogeneous nanoparticles, hence prolonging their lifetime, which can improve the photoconductive gain and photocurrent.

## 1D nanomaterials

Unlike 0D quantum dots, 1D nanomaterials (including nanowires, nanotubes and nanorods) are confined only in two dimensions, and charge carriers propagate freely along the third dimension<sup>60</sup>. 1D nanowires featuring large aspect ratios are suitable for fabricating photonic platforms, such as interconnects and waveguides. These building blocks with several-micrometre-lengths bridge the nanoscopic and macroscopic worlds, creating possibilities for designing high-performance optoelectronic devices<sup>61</sup>.

The efficient transport of charge carriers in one dimension can generate a continuous photoconductivity effect (corresponding to high photoconductive gain). In addition, a 1D carrier transport mode makes charge collection more efficient in the most basic photoconductor-type photodetector structure<sup>62</sup>. Meanwhile, the distinct high aspect ratio of 1D nanomaterials gives them an unexpectedly high absorption cross-section, enhancing their capacity for sufficient photon harvest<sup>63,64</sup>. Especially in the short wavelength region (covering the UV region) (Fig. 3e), 1D nanomaterials have an inherent antireflection effect compared with their analogous thin-film structure, laying a foundation for high-responsivity UV photodetectors<sup>65</sup>. Given their notable photon absorption and transport and collection of charge carriers, 1D materials are better able to maximize the use of photons and improve responsivity compared with their thin-film-structure counterparts.

To date, photodetectors based on a single 1D nanomaterial have achieved a high responsivity<sup>66</sup>. However, they display weaker

photocurrent signals than their corresponding large-area photodetectors, because the area of the 1D material is constrained by its nanoscale diameter (merely 2–200 nm)<sup>61</sup>. The photocurrent can be improved by placing multiple nanowires side-by-side lengthwise, which would increase both the light-absorbing area of the photodetector and the number of channels for charge carrier transport and collection. For example, several bridged Ga<sub>2</sub>O<sub>3</sub> nanowires were efficiently assembled into one photodetector, establishing parallel charge transport channels and increasing the photocurrent output<sup>67</sup>. It is worth noting that the orientation of nanowires to each other is also important, and photodetectors based on arrayed 1D nanomaterials have been developed. For example, ordered and high-density vertical titanium dioxide (TiO<sub>2</sub>) nanotube arrays enable a large photocurrent, because charge carriers are efficiently transported and collected vertically through the ordered arrays<sup>68</sup>.

In addition, axial (double junction) or radial (core–shell) heterojunctions can be constructed in 1D materials to provide a built-in electric field and endow the device with self-powered performance<sup>69–71</sup> (Fig. 3f). The built-in electric field can prevent the injection of charge carriers in the dark state and suppress the dark current; photogenerated electron–hole pairs can be separated and transported under the function of the internal electric field, without additional applied voltage. This self-powered photodetector can eliminate dependence on a power supply and adapt to application scenarios requiring high integration and portability. At present, limited by inefficient charge collection strategies, the maximum self-powered photocurrent of UV photodetectors based on 1D heterojunction arrays can reach only nanoscale amperes (nA)<sup>69,72</sup>.

## 2D nanomaterials

As the thickness of a bulk material (such as Si or Ge) is reduced to several nanometres, surface and internal defects will inevitably diminish the carrier mobility of the material<sup>73</sup>. Unlike bulk materials, 2D semiconductors (including nanosheets, nanobelts, monolayers or bilayers and quasi-2D films or nanomembranes) can maintain a high carrier mobility under atomic-scale thickness, owing to passivated surfaces that are free of dangling bonds, minimizing the scattering effect<sup>74</sup>. Benefiting from the ultrathin 2D material, the carriers can be effectively controlled by introducing gate voltage and thus can suppress the noise current of the device and reduce the power dissipation of the photodetector.

In 2D materials, atoms are strongly connected within planes by covalent bonds, whereas they are weakly associated between layers through vdW forces. 2D materials can be transferred onto almost any substrate to realize monolithic integration regardless of lattice mismatch. This type of vdW integration can easily combine 2D materials of different dimensions, crystal structures or electronic properties<sup>75</sup> without lattice and processing constraints and is a common strategy to improve the responsivity, detectivity and response speed of a photodetector.

However, most 2D semiconductors, such as metal dichalcogenides<sup>76</sup>, black phosphorus<sup>77</sup> and graphene<sup>57</sup>, are not competitive for the detection of UV light, especially solar-blind deep-UV light, owing to their relatively small bandgap (<2.5 eV). Searching for 2D WBSs for UV detection has been an important topic. 2D h-BN has been developed as a deep-UV-light-sensitive semiconductor given its large bandgap of about 6 eV and high absorption coefficient of about  $7 \times 10^5 \text{ cm}^{-1}$

## Box 1

### Performance metrics for UV photodetectors

#### Responsivity

Responsivity ( $R_\lambda$ ) is the most basic performance metric of a photodetector. It describes its optoelectronic conversion capability, given by the equation:

$$R_\lambda = \frac{I_{ph}}{PS}$$

$P$  is the light power density of the incident light and  $S$  represents the area of the photodetector. The photocurrent ( $I_{ph}$ ) of the photodetector determines its  $R$  when fixing  $P$  and  $S$ . On the basis of the working process of the photodetector, the photocurrent can be enhanced by improving the photon absorption capacity, improving the charge separation and transport efficiency and improving the collection efficiency of carriers of the device.

#### Specific detectivity

Specific detectivity ( $D^*$ ) is not only related to the photoresponse of a photodetector under illumination but also related to its current signals in a dark state, which can be evaluated by the capability of a photodetector to detect the weakest light. It is a comprehensive indicator, defined by the equation<sup>146,147</sup>:

$$D^* = \frac{\sqrt{A\Delta f}}{NEP}$$

$$NEP = \frac{I_N}{R_\lambda}$$

in which  $A$  represents the active area of the device ( $\text{cm}^2$ ),  $\Delta f$  (Hz) is the electrical bandwidth of the noise measurement, NEP is the noise-equivalent power and  $I_N$  is the noise current. There are three main sources of noise, including shot noise, Johnson (thermal) noise and flicker noise.  $D^*$  cannot be calculated simply through dark current (basically corresponding to shot noise), which may result in a larger estimation than the actual value. In addition, dark current can be effectively suppressed by defect engineering<sup>148–150</sup> and device engineering strategies<sup>151,152</sup>. Meanwhile, under some extremely weak light detection circumstances (such as single-photon detection), it is necessary to minimize the interference of thermal noise to the output photoresponse signal of the photodetector by lowering temperature.

#### Response speed

Response speed of a photodetector can be evaluated by the response time (rise time and decay time) or  $-3\text{dB}$  bandwidth. In most cases, response speed is mainly restricted by the decay time, which is bound up with the recombination process of charge carriers as light switches off.

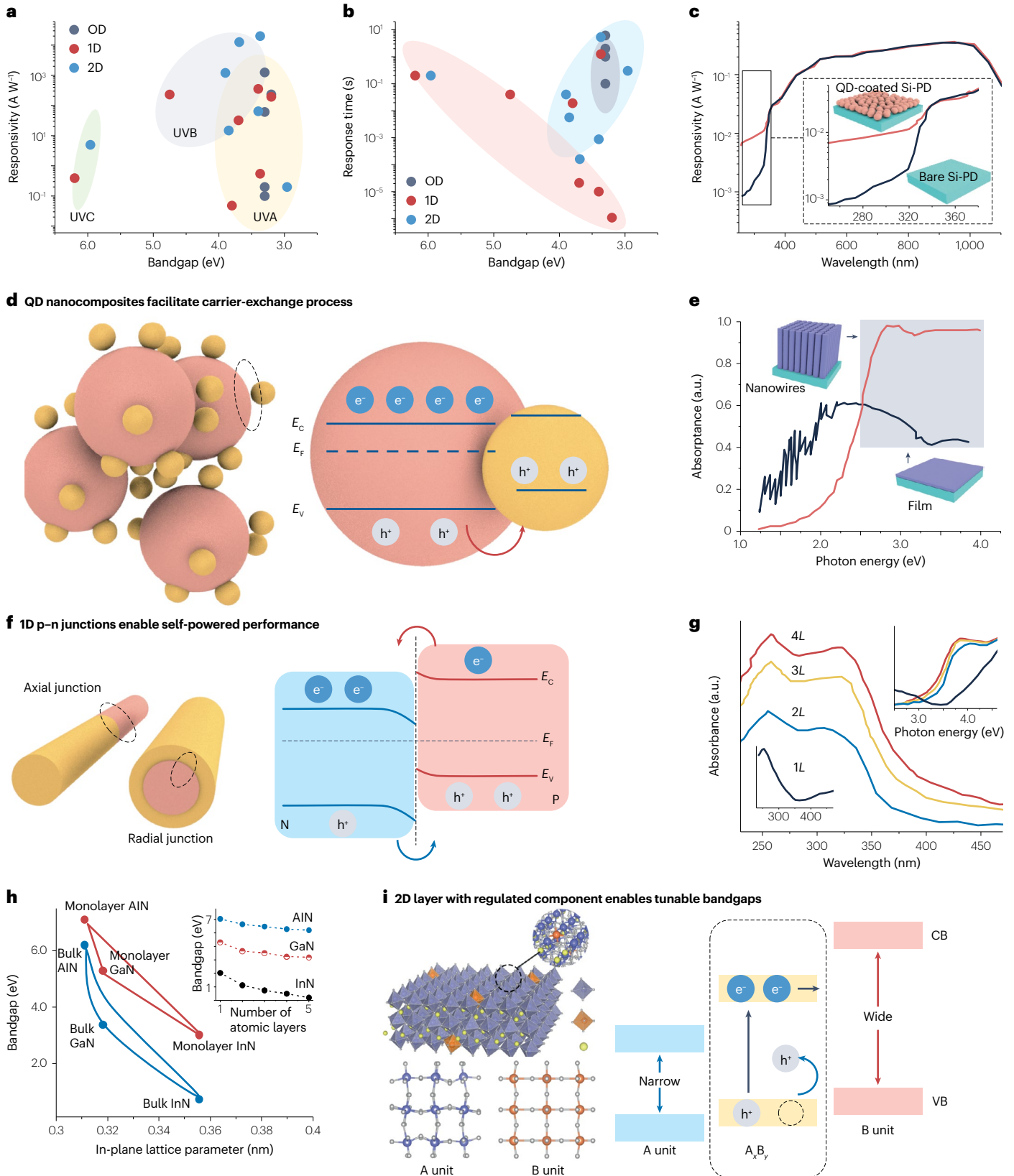




**Fig. 3 | Dimensionality engineering and tunable optoelectronic performance.** **a**, UVC photodetectors (especially deep-UV photodetectors) display a responsivity almost three to four orders of magnitude lower than that of UVB and UVA photodetectors. The data are from Table 2. **b**, Photodetectors based on 1D or 2D materials can obtain relatively fast response times of several microseconds, whereas 0D materials suffer from response times as slow as several milliseconds or even seconds. The data are from Table 2. **c**, UV-sensitive quantum dots can be coated on an Si photodetector to enhance its UV photoresponse and will not affect its responsivity to visible-near IR light<sup>54</sup>. **d**, Wide-bandgap quantum dots can be decorated with other quantum dots to facilitate the carrier-exchange process through energy band regulation<sup>59</sup>. **e**, By rationally designing the wire diameter, length and filling ratio, 1D nanowire arrays can have higher absorptance than their film counterpart in the UV-wavelength region<sup>65</sup>. **f**, Self-powered performance in

a photodetector can be obtained by constructing a nanowire heterojunction<sup>68</sup>. **g**, The bandgap of a 2D material can be regulated by its number of layers ( $L$ )<sup>82</sup>. **h**, Diagram of bandgap versus in-plane lattice parameter from bulk to monolayer in III-nitrides. The inset is the bandgap variation with the number of atomic layers<sup>85</sup>. **i**, The bandgap of a 2D material can be tuned by component design, including introducing substituted ions or changing their compositions. Here, A unit refers to  $\text{Ca}_2\text{Nb}_3\text{O}_{10}$ , B unit refers to  $\text{Ca}_2\text{Ta}_3\text{O}_{10}$  and  $\text{A}_x\text{B}_y$  refers to  $\text{Ca}_2\text{Nb}_{3-x}\text{Ta}_x\text{O}_{10}$ , where  $\text{Nb}^{5+}$  ions are partially substituted by  $\text{Ta}^{5+}$  (ref. 83). CB, conduction band; PD, photodetector; QD, quantum dot; VB, valence band. Panel c adapted with permission from ref. 54, Wiley. Panel e adapted with permission from ref. 65, copyright 2007 American Chemical Society. Panel g adapted with permission from ref. 82, Wiley. Panel h reprinted from ref. 85, Springer Nature Limited.

(refs. 78,79); however, it has long suffered from low responsivity. One solution is to introduce metal (such as Au and Al) nanoparticles onto the surface of h-BN nanosheets to create vdW integrations where localized surface plasmon resonance effects will be produced, augmenting UV light absorption<sup>48</sup>. The fabricated vdW integrations promote the separation of photogenerated carriers, thus enhancing the photocurrent and responsivity of the photodetector<sup>48,80</sup>. Nevertheless, h-BN performs far from satisfactorily for deep-UV photodetection, with a maximum responsivity of about  $5 \text{ A W}^{-1}$  and an undesirably high dark current density of  $0.6 \mu\text{A cm}^{-1}$  (refs. 2,49); thus, it is necessary to discover alternative materials to achieve the optimal balance between responsivity and detectivity (dark current).

A series of ternary 2D semiconductors with tunable bandgaps, made by varying the material stoichiometry, is an exciting development in UV detection<sup>81–83</sup>. Changing the number of layers of the 2D semiconductors can also control the bandgap (Fig. 3g), allowing the detection of light with different wavelengths<sup>84</sup>. Figure 3h demonstrates the variation in bandgap with the lattice parameter and number of atomic layers in III-nitrides<sup>85</sup>. The bandgap of III-nitride increases with decreasing number of atomic layers. Monolayer AlN, with the smallest lattice parameter, exhibits the greatest bandgap of up to 7.0 eV. Previous studies have demonstrated that a relatively narrow bandgap is often caused by excessive thickness of the material, so fabricating high-quality ultrathin nanoflakes is an inevitable way to obtain a wide bandgap<sup>86</sup>. For example, BiOBr, whose bandgap was 2.65 eV in a thick sample, achieved its largest bandgap of 3.69 eV when its number of layers was tailored to 1 (0.57-nm thick). A photodetector based on this monolayer delivered a remarkable deep-UV detecting performance with an ultrahigh responsivity ( $12,739.13 \text{ A W}^{-1}$ ), ultrahigh EQE ( $6.46 \times 10\%$ ) and superb detectivity ( $8.37 \times 10^{12}$  Jones) under 245 nm with a  $-35\text{-V}$  photogating control<sup>82</sup>. In addition, the bandgap of a 2D material can be tuned by component design. For example,  $\text{Ca}_2\text{Nb}_3\text{O}_{10}$  nanosheets can realize tunable bandgaps by B-site cation substitution, in which  $\text{Nb}^{5+}$  is partially substituted by  $\text{Ta}^{5+}$  to form  $\text{Ca}_2\text{Nb}_{3-x}\text{Ta}_x\text{O}_{10}$  solid solutions (Fig. 3i).

## Device design

Device design principles can optimize the performance of UV photodetectors. A graphene charge-injection photodetector integrates three functionalities to broaden the detection bandwidth and simplify the readout process<sup>87</sup> (Fig. 4a). The device structure includes single-layer graphene for non-destructive direct readout and multilayer graphene for IR photocharge injection. Upon light illumination, a photothermionic emission process is generated, leading hot holes to be injected

from the multilayer graphene layer to n-type Si (Fig. 4b). Photocarriers are then stored in deep-depletion wells at the voltage pulse. Finally, the top single-layer graphene directly reads out the stored carriers through a photogating effect. This design of phototransistor incorporates low-dimensional graphene and deep-depletion wells to enhance the responsivity in a controllable way. Overall, this device combines the independent pixel structure of a complementary metal-oxide semiconductor (CMOS) and the charge integration feature of a charge-coupled device (CCD).

A bipolar junction phototransistor can switch or amplify electronic signals in integrated circuits and can be realized through multijunction or tandem strategies in energy-harvesting optoelectronic devices<sup>88</sup>. A bipolar UV photodetector based on p-AlGaIn/n-GaN nanowire arrays on an n-type Si(111) substrate was reported<sup>71</sup>. An individual nanowire comprises an axially aligned Mg-doped p-AlGaIn segment and an Si-doped n-GaN segment in an electrolyte environment (Fig. 4c). In this device architecture, the top p-AlGaIn part is designed to absorb high-frequency photons (deep-UV light), and the bottom n-GaN segment can absorb low-frequency photons (lower-energy light). Furthermore, the relatively small band offset provides efficient carrier transport between the n-GaN and n-Si conduction band edges. Upon 254-nm illumination, electron–hole pairs are generated in both p-AlGaIn and n-GaN segments (Fig. 4d). Electrons of the p-AlGaIn side facilitate the proton reduction reaction, whereas the electrons and holes recombine in the space charge region. Thus, the remaining holes in the n-GaN side migrate under the effect of the external circuit, leading to a negative photocurrent signal. Upon 365-nm illumination, the holes facilitate the oxygen evolution reaction, while the remaining electrons drift towards the external circuit, thus exhibiting a positive photocurrent signal. Clearly, the two bipolar photoresponses have entirely different operation mechanisms at the nanowire–electrolyte interface. Bipolar phototransistors are believed to have potential for reconfigurable neural network vision sensors<sup>89</sup>.

A negative photoresponse, in which the current decreases after illumination, is an abnormal optoelectronic phenomenon<sup>90</sup>. Negative UV photoconductivity observed in vertical ZnO nanowires was originally ascribed to the electron trapping in the alumina membrane<sup>91</sup>. However, owing to the slow progress in developing devices with negative UV photoresponse, more work must be done to further determine the working mechanism. As one example, a working mechanism was proposed for the negative UV phototransistor in few-molecular-layer 2D crystals<sup>90</sup>. The device exhibits a typical n-type transistor performance under a positive gate voltage and dark conditions and a lower current under UV illumination (Fig. 4e). Under UV light illumination,

**Table 2 | Figures of merit and progress of UV photodetectors based on low-dimensional wide-bandgap semiconductors**

Dimension	Material	Growth method	Bandgap (eV)	Wavelength (nm)	$R_{\lambda}$	$D^*$ (Jones)	Response time	Applied voltage (V)	Year	Ref.
0	ZnMgO nanoparticle-coated Si	Solution method	4.22	260	$7.5\text{mA W}^{-1}$				2022	54
	Cu nanostructures + ZnO quantum dots	Solvothermal method	3.2	365	$234\text{A W}^{-1}$		7.4/29s	10	2019	131
	ZnO quantum dots	Femtosecond-laser ablation in liquid	3.3	224	$100\text{mA W}^{-1}$		70ms	5	2018	55
	ZnO nanoparticles + Au nanoantennas	Solvothermal method	3.3	365	$\sim 200\text{mA W}^{-1}$	$3.6 \times 10^{12}$	3.55/1.49s	10	2018	132
	ZnO quantum dots + graphene	Solvothermal method	3.4		$9.9 \times 10^8\text{A W}^{-1}$	$10^{14}$	5/85.1s	10	2017	133
	Graphdiyne + ZnO nanoparticles	Solution preparation	3.2	365	$1,260\text{A W}^{-1}$		6.1/2.1s	10	2016	59
	ZnO nanoparticles	Flame spray pyrolysis	3.37	300–400	$13\text{A W}^{-1}$		200/150s	5	2015	50
	ZnO nanoparticle-polymer blend	Hydrolysis method	3.4	360	$1,001\text{A W}^{-1}$	$3.4 \times 10^{15}$	142/558 $\mu\text{s}$	9	2012	56
	ZnO nanoparticles	Solvothermal method	3.35	370	$61\text{A W}^{-1}$		<0.1s/1s	120	2008	51
1	TiO <sub>2</sub> nanorod arrays + Ti <sub>3</sub> C <sub>2</sub> T <sub>x</sub> /Au	Hydrothermal synthesis methods	3.2	370	$195\text{A W}^{-1}$	$4.3 \times 10^{13}$	1.08 $\mu\text{s}$	–1.5	2023	134
	<i>n</i> -AlGa <sub>N</sub> nanowires + <i>n</i> -Ga <sub>N</sub> nanowires	Plasma-assisted molecular beam epitaxy	3.82/3.4	254	$3.7\text{mA W}^{-1}$			0	2021	70
	Arrayed ZnO–CuO core–shell nanorods + Au nanoparticles	Hydrothermal method	3.37	325	$0.14\text{mA W}^{-1}$	$3.3 \times 10^{11}$	10ms	0	2021	69
	CsCu <sub>2</sub> I <sub>3</sub> nanowires	Antisolvent method	3.73	250–350	$32.3\text{A W}^{-1}$	$1.89 \times 10^{12}$	6.94/214 $\mu\text{s}$	5	2020	135
	Y <sup>3+</sup> -doped TiO <sub>2</sub> nanofibres	Electrospinning		350	$4.5\text{A W}^{-1}$	$1.6 \times 10^{11}$	2.53/1.16s	3	2020	98
	AlGa <sub>N</sub> nanowires	Plasma-assisted molecular beam epitaxy		254	$48\text{mA W}^{-1}$		83/19ms	0	2020	136
	$\beta$ -Ga <sub>2</sub> O <sub>3</sub> nanowires	Vapour–solid synthesis	4.75	<300	$233\text{A W}^{-1}$	$8.16 \times 10^{12}$	0.48/0.04s	10	2019	137
	Single-nanowire Ga <sub>N</sub>	Plasma-assisted molecular-beam epitaxy	3.4	<370	$355\text{A W}^{-1}$		~10 $\mu\text{s}$	3	2019	66
	ZnO–Al <sub>N</sub> core–shell nanowires	Vapour phase transport		325	$2.05 \times 10^4\text{A W}^{-1}$		28ms	5	2019	138
	<i>p</i> -CuZnS/ <i>n</i> -TiO <sub>2</sub> arrays	Anodic oxidation process	3.2	300	$2.54\text{mA W}^{-1}$		<0.2s	0	2018	68
	ZnO nanorods	Hydrothermal synthesis methods	3.37	365	$0.55\text{A W}^{-1}$		3.1/1.25s	10	2017	139
	Al <sub>N</sub> micro-nanowire	Physical vapour transport	6.2	190	$0.39\text{A W}^{-1}$		0.1/0.2s	20	2015	23
	Parallel arrayed ZnO nanowires	All-printable fabrication		365	$7.5 \times 10^6\text{A W}^{-1}$	$3.3 \times 10^{17}$		1	2014	62
	Bridged $\beta$ -Ga <sub>2</sub> O <sub>3</sub> nanowires	Chemical vapour deposition	4.5	<280			<<20ms	50	2010	67
2	h-BN + Al nanoparticles	Metal organic vapour phase epitaxy	5.96	205	$12\mu\text{A W}^{-1}$			10	2022	48
	$\gamma$ -Bi <sub>2</sub> O <sub>3</sub> flakes	Chemical vapour deposition	3.4	365	$64.5\text{A W}^{-1}$	$1.3 \times 10^{13}$	290/870 $\mu\text{s}$	5	2022	84
	h-BN 2D nanosheets + Cu	Solid state-assisted synthesized	6	210	$5.022\text{A W}^{-1}$	$6.1 \times 10^{12}$	200ms	5	2021	49

**Table 2 (continued) | Figures of merit and progress of UV photodetectors based on low-dimensional wide-bandgap semiconductors**

Dimension	Material	Growth method	Bandgap (eV)	Wavelength (nm)	$R_{\lambda}$	$D^*$ (Jones)	Response time	Applied voltage (V)	Year	Ref.
2 (continued)	Ca <sub>2</sub> Nb <sub>3</sub> O <sub>10</sub> flakes	High-temperature solid-state reaction and liquid exfoliation	3.85	280	14.94 A W <sup>-1</sup>	8.7×10 <sup>13</sup>	0.08/5.6 ms	3	2021	140
	Ca <sub>2</sub> Nb <sub>2.5</sub> Ta <sub>0.5</sub> O <sub>10</sub> nanosheets	High-temperature solid-state reaction and liquid exfoliation	3.65	295	469.5 A W <sup>-1</sup>	8×10 <sup>13</sup>	0.9/152 ms	1	2021	83
	AlGaIn + GaN	Metal organic chemical vapour deposition		365	1,670 A W <sup>-1</sup>		0.05/0.36 s		2021	141
	Sr <sub>2</sub> Nb <sub>3</sub> O <sub>10</sub> nanosheets	High-temperature solid-state reaction and liquid exfoliation	3.9	270	1,214 A W <sup>-1</sup>	1.4×10 <sup>14</sup>	0.4/40 ms	1	2020	86
	BiOBr nanoflakes	Chemical vapour deposition	3.69		12,739.13 A W <sup>-1</sup>	8.37×10 <sup>12</sup>	110/160 μs	10	2020	82
	ZnO nanosheets	Soft template-assisted growth	3.37	254	20,000 A W <sup>-1</sup>	6.83×10 <sup>14</sup>	3.97/5.32 s		2020	142
	BiOCl flakes	Chemical vapour deposition	3.5	250	35.7 A W <sup>-1</sup>	2.2×10 <sup>10</sup>		1	2020	143
	GeSe <sub>2</sub>	Chemical vapour transport	2.96	266	200 m A W <sup>-1</sup>	1.6×10 <sup>15</sup>	214/304 ms	10	2019	144
	Diamond film	Chemical vapour deposition	5.5	220	6 A W <sup>-1</sup>			3	2006	145

$D^*$ , specific detectivity; h-BN, hexagonal boron nitride;  $R_{\lambda}$ , responsivity.

electron–hole pairs are generated and then separated at the heterojunction interface (Fig. 4f). Later, the majority of carriers are transferred and recombined with the gate-induced electrons, leading to a substantial current decrease. When the channel layer contains dozens of molecular layers, the electrons near the interface are recombined but many residual electron carriers remain, resulting in considerable positive current and poor negative current. Negative UV phototransistors have potential in fabricating light encoders, which can encrypt electrical signals by light.

## Applications

### Flexible electronics

Bulk inorganic semiconductors are often mechanically rigid owing to their strong covalent bonding and moderate thickness. Reducing the size of at least one dimension to hundreds or even tens of nanometres will improve the flexibility of the material<sup>92–94</sup>. Furthermore, compared with soft organic semiconductors, inorganic low-dimensional WBSs have better environmental stability (including to oxygen, steam and temperature) and mechanical wearing resistance<sup>86,95</sup>.

Two-dimensional WBSs with layered and non-layered structures are composed of single or several stacked atomic layers and are extremely thin, which endow them with good elasticity and adhesion<sup>96</sup>. They can be transferred onto flexible substrates or directly onto human skin to realize free-standing skin electronics<sup>34,97</sup>. Two-dimensional WBSs keep close and imperceptible contact with skin, so they can monitor high-fidelity biological signals for a long time without disturbing the daily activities of the wearer and may enable remote monitoring of accurate health in the future. As an example of such a biomedical sensing platform, a low-power-consumption, high-sensitivity, stretchable electronic skin was fabricated on the basis of ultrathin single-crystalline GaN films. This chip-less, wireless sensor presented an outstanding

spectral selectivity responsivity of 10.06 A W<sup>-1</sup>. Owing to its ultrathinness (around 300 nm), the electronic skin has improved softness and comfort, and less power waste, compared with a relatively thick skin device (300–500 μm)<sup>97</sup>.

One-dimensional WBSs, with nanoscale diameters and macroscale lengths, have excellent bending performance<sup>95</sup>. A wearable macroscopic 3D flexible device based on 1D nanotubes can be realized through direct anodic oxidation of Ti microwires<sup>68</sup>. Similarly, free-standing fibrous membranes based on TiO<sub>2</sub> nanowires can be prepared directly from a TiO<sub>2</sub> precursor solution by electrostatic spinning technology; their mechanical flexibility can be improved by component doping engineering<sup>98</sup>. Nanofibre membranes are also breathable, effectively reducing skin inflammation in epidermal electronics applications<sup>99</sup>. In addition, in many application scenarios (such as electronic skin and motion detection), a photodetector will bear tensile, compression and twisting forces, so it must be stretchable to avoid serious damage to performance from device breakage. One strategy to achieve a balance between flexibility and optoelectronic performance is to randomly distribute interpenetrating networks of 1D WBSs in an elastic matrix (such as polydimethylsiloxane, styrene–ethylene–butylene–styrene or thermoplastic polyurethane). The functional WBSs provide UV photodetection, and the elastic matrix endures the tensile stress<sup>94</sup>. As this device is stretched, it corresponds microscopically to a large number of flexible nanowires bearing bending stress. However, a single nanowire cannot achieve axial stretching because its atoms in the axial direction are tightly bound by strong covalent bonds.

### UV imaging

UV imaging technology is an effective supplement to the spectral response range of current commercial visible light cameras, and it has important application prospects in space UV optical remote sensing,

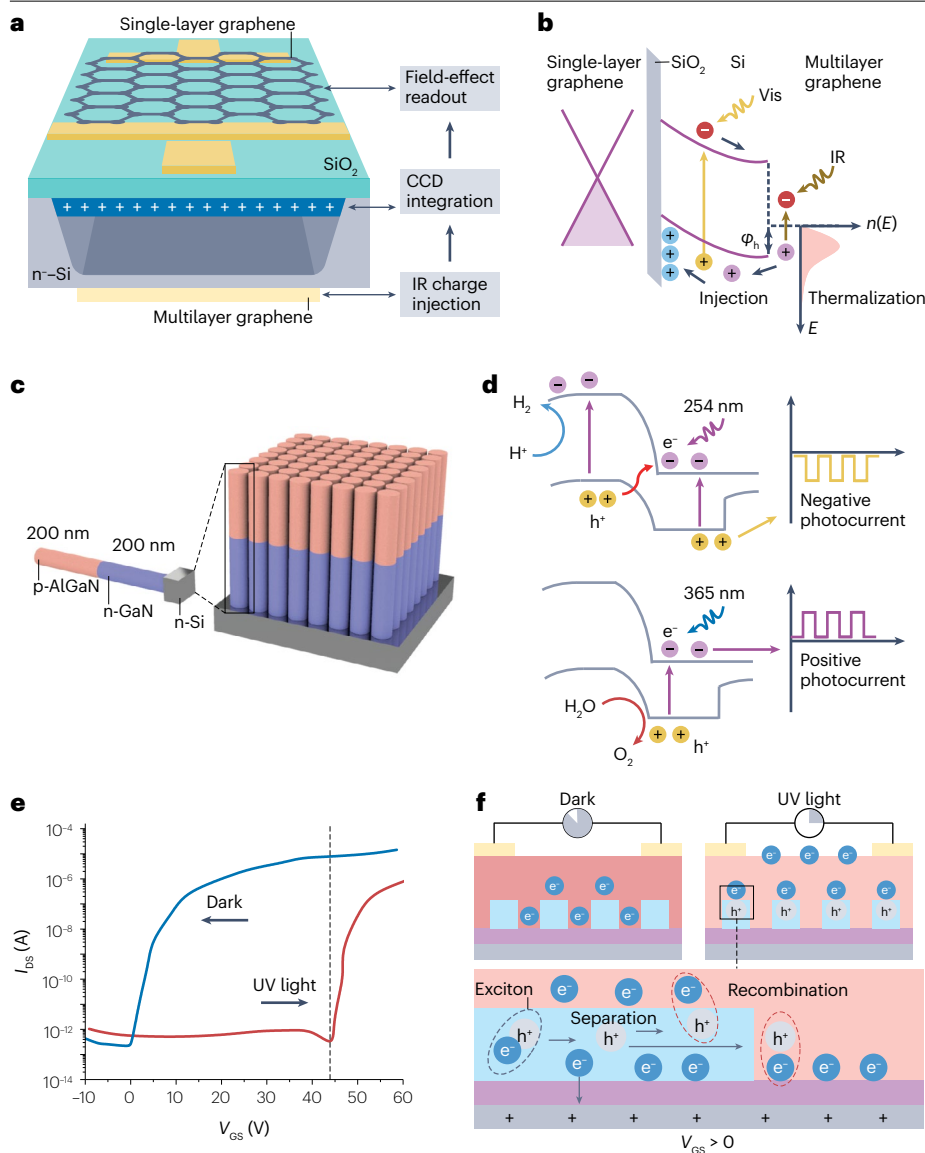


**Fig. 4 | Device designs for UV photodetectors.**

**a**, Schematic illustration of a graphene charge-injection photodetector, which consists of multilayer graphene for infrared (IR) charge injection, single-layer graphene for direct non-destructive field-effect readout and a deep-depletion silicon well for charge integration. **b**, Band diagram and carrier movement of graphene charge injection. The thermalized hot carriers are injected into silicon under IR light illumination, and the visible light-excited holes are integrated in the silicon well<sup>87</sup>. **c**, Schematic of the p-AlGaIn/n-GaN nanowires on n-Si substrate<sup>71</sup>. **d**, Band diagram and operation model of the p-AlGaIn/n-GaN nanowire photodetector with light-induced photocarrier excitation, recombination and diffusion processes. Under 254-nm illumination, a negative photocurrent signal is obtained owing to proton reduction at the p-AlGaIn surface. Under 365-nm illumination, a positive photocurrent signal is generated owing to water oxidation at the n-GaN surface<sup>71</sup>. **e**, Transfer curves of 1D/2D molecular crystal p-n heterojunctions under light and dark conditions. The current is higher without light illumination, owing to the negative photoresponse. **f**, Schematic illustration of the p-n heterojunction under light and dark conditions and of the negative optoelectronic process. Under UV light illumination, electron-hole pairs are generated and the excitons are separated at the heterojunction interface<sup>90</sup>. CCD, charge-coupled device; DS, drain source; GS, gate source; Vis, visible. Panels **a** and **b** reprinted from ref. 87, Springer Nature Limited. Panels **c** and **d** reprinted from ref. 71, Springer Nature Limited. Panels **e** and **f** reprinted with permission from ref. 90, Wiley.

close-range criminal investigation and photography<sup>100,101</sup>. CCDs and CMOSs are widely incorporated into imaging sensor technology. Owing to the disadvantages of limited readout speed, high fill factor, high power consumption and high cost in CCD imaging sensors, CMOS technology is more popular in UV imaging applications. A CMOS-integrated 64-pixel UV imaging sensor based on a wide-bandgap SiC semiconductor achieved readout times down to 0.39 Hz and power consumption as low as 60  $\mu$ W (ref. 24).

At present, high resolution is an important goal for imaging technology and depends on the integration of high-density photosensitive devices. In high-density arrayed 1D nanomaterials, a single nanowire or nanotube can function as a photosensitive pixel. If the photocurrent signals in each nanowire can be electrically addressed, this type of densely arrayed device may exceed the highest resolution of the most advanced CCD or CMOS image sensor<sup>102</sup>. However, it remains difficult to electrically address individual 1D materials.

Two-dimensional materials can avoid this problem by being transferred onto a CMOS-based silicon integrated circuit to realize monolithic integration. In this case, large-area, uniform and isotropic 2D materials are necessary to ensure the accuracy of the image. In addition, combining flexible low-dimensional materials and imaging technology can enable flexible UV imaging devices. For example, an artificial retina, enabled with flexible UV imaging, can achieve wider angle image recognition<sup>103</sup>.

Meanwhile, single nanowire or small-area 2D semiconductors have application prospects in the field of single-pixel imaging<sup>104</sup>. A single pixel can provide high-resolution UV imaging by relying on the movement of the light spot to image the entire object<sup>105</sup>. Compared with a camera based on CMOS or CCD technology, single-pixel imaging has the advantages of simple readout circuit and no required compatibility with silicon. The imaging pixel is not restricted by the density of the photo sensors and is only related to the size of the spot and of the



moving path. The disadvantage is that it is a kind of scanning imaging, which needs to read the optical current point by point, resulting in a slow imaging speed.

## Weak UV light detection

The ability to detect weak light makes it possible to observe at a longer distance or in an environment in which photons are scarce, such as in ultralow power remote sensing, night operation and obtaining high-resolution 3D images from a far distance. The difficulty in realizing the detection limit of photodetectors makes weak light detection a challenge. There are three possible solutions: to improve the absorption probability of photons (even total absorption of photons), to find an appropriate charge gain mechanism and to reduce the noise level (mainly thermal noise).

Experimental and theoretical studies show that vertically oriented nanowires can become nearly perfect absorbers if designed with appropriate nanowire parameters (length, diameter and spacing) and can have nearly uniform absorption efficiency in a wide wavelength range<sup>106</sup>. For example, by designing an array of conical nanowires (in which the size of the tip is smaller than the bottom) and optimizing the spacing between the nanowires, photon absorption is maximized<sup>107</sup>. Therefore, although the thickness and volume of the nanowire array are much smaller than those of its corresponding film, the absorption at some resonance wavelengths can even exceed that of the film<sup>65</sup>. In addition, owing to the volume reduction, the dark current of the nanowire arrays will be smaller than that of the film, which is conducive to photon detection at room temperature<sup>62,107</sup>.

The construction of a heterojunction can function as a high resistance state in the space charge region (built-in electric field) and can effectively suppress the current in the dark state<sup>63</sup>. By further utilizing the avalanche effect of photodiodes, high gain can be obtained to detect weak light. In addition, 2D materials have atomic layer thickness and no dangling bond interface, and nanoscale vdW heterostructures can be fabricated. The nanoscale 2D/2D heterostructure has a short effective region located in the sub-average free path region, so that it can realize ballistic avalanche without phonon scattering. This is conducive to increasing multiplication factor and reducing excess noise, thus realizing the detection of weak light<sup>26</sup>. Therefore, low-dimensional WBSs are suitable candidate materials to achieve weak UV light detection.

## Multispectral photodetection

Distinguishing among UVA, UVB and UVC light is important for carrying out the best prevention or application of UV radiation.

One way to realize UV spectrum recognition is inspired by the design of currently commercialized colour cameras. Colour imaging is attained when photons pass through colour separation filters and are converted into electronic signals through wideband-response Si photodetectors. Similarly, spectrum recognition of UV light can be realized by integrating UV narrowband filters with a full-UV-band response photodetector on one chip. It remains a challenge to develop a full-UV-band response photodetector from one semiconductor, so low-dimensional materials with different UV spectrum response ranges can be transferred onto a single chip to achieve full-UV-band detection. The advantage of this method is that it can recognize multiple UV bands as long as there are appropriate UV filters and simultaneously perform both UV intensity measurement and spectrum recognition. The disadvantage is that the integration of multiple semiconductors makes the device structure complex.

Another strategy is based on the special optoelectronic properties of low-dimensional UV photodetectors. Generally, current flows unidirectionally. However, in multijunction devices based on 1D materials, bipolar directional current output is possible by combining the principles of optoelectronic conversion, optoelectronic chemical conversion and photothermal conversion<sup>108–110</sup>. Under the irradiation of excitation light with different UV wavelengths, this type of device can generate distinguished photocurrent signals with opposite polarities, so as to differentiate within the UV spectrum<sup>71,108</sup>. The advantages of this method are that the device structure is simple, and the intensity of UV light can be measured. The disadvantage is that it can only distinguish narrow UV bands.

The third way is to take advantage of the complete optoelectronic and photoluminescence characteristics of wide-bandgap quantum dots and integrate them on a CMOS Si image sensor<sup>54</sup>. Given the efficient luminescence and large Stokes shift of quantum dots, they can be used as a down-conversion material to convert the UV light into visible light. Meanwhile, wide-bandgap quantum dots have compositionally tunable bandgaps, and the colour of their spectral emission depends on the wavelength of UV excitation. The UV spectrum can be recognized by stacking UV-photosensitive quantum dots with different bandgaps. Simultaneously, converting UV light into visible light can enhance the responsivity of Si photodetectors in the UV region. The advantage of this method is that UV light can be easily and directly recognized by the human eye by converting it into visible light, and the quantum dot is compatible with CMOS circuit integration. The disadvantage is that the accuracy of spectrum recognition is low and there are individual differences in distinguishing different colours.

Traditional UV photodetectors cannot acquire the complicated information in a complex environment that is often needed for applications. Low-dimensional WBSs may enable high-performance UV photodetectors with multidimensional functions, owing to their scalable UV absorption, tunable performance and distinctive anisotropic optical property<sup>111</sup>. These multidimensional features include not only multispectral photodetection but also the ability to capture abundant light information including polarization, phase and optical path. Developing UV photodetectors with multidimensional features will likely be a mainstream trend in this intelligent era.

## Challenges and outlook

Nowadays, UV photodetectors are not only recognized as a light-function device to transfer optical signals but also serve as an important component in optoelectronic integration circuits, which also include electronic components, optical waveguides and light-emitting diodes on the chip. However, there is still plenty of room to develop UV photodetectors towards weak-light photodetection, high-gain (responsivity, noise equivalent power and quantum efficiency) devices, transparent and flexible electronics and photonics.

## Discovery and engineering of low-dimensional WBSs

With advances in synthetic methods, the library of WBSs has been enriched to include bulk crystal and few-layer 2D materials involving carbides, nitrides, oxides, chalcogenides and halides, among others. These materials cover the bandgap range from 3.2 eV to 7.3 eV (Fig. 5a), making them promising candidate semiconductors for next-generation UV photodetection technology. Filterless vacuum UV photodetectors in particular are expected to adopt ultrawide bandgap semiconductors<sup>12,23</sup> (more than 6 eV). Therefore, it is desirable to discover many more wide-bandgap semiconductors with low-dimensional

structure. Another challenge in material design is that high-mobility, p-type WBSs are still lacking. Exploring highly conductive p-type and n-type low-dimensional WBSs is being pursued at the same time to make progress in the near future<sup>112</sup>.

Furthermore, in a given UV radiation, it is a challenge to accurately differentiate the proportion of UVA, UVB and UVC wavelengths, each of which is strongly associated with human health and industrial activities<sup>113</sup>. The main problem lies in realizing spectral narrowband photoresponse in a UV photodetector. Although some strategies (charge collection narrowing, organic additives and stacked device structure) have enabled narrowband photodetection, there remains plenty of room to design narrowband UV photodetectors on the basis of WBSs. By controlling the number of atomic layers and thus regulating the absorption wavelength, an ultranarrow deep-UV photoresponse down to 9 nm was achieved in a low-dimensional  $(\text{AlN})_m/(\text{GaN})_n$  superlattice photodetector<sup>114,115</sup>. Therefore, accurately controlling the thickness of WBSs will be key to the development of narrowband UV photodetectors.

Engineering the low-dimensional structure of WBSs creates lots of opportunity to actualize integrated nanoscale optoelectronics. Assembly of OD colloidal nanocrystal quantum dots is a method to obtain tailored electronic properties, such as mobility, carrier density

and bandgap. The nanocrystal packing can also lead to semiconductors with anisotropic electronic properties and isotropic optical properties or vice versa. One-dimensional nanowire techniques introduce a small epitaxial interface even under high lattice mismatch, which brings high-quality single-crystalline materials and a sub-femtofarad capacitance for both high-speed and low-power operation. Ultrathin 2D semiconductor layers are potentially attractive for fabricating miniaturized and fast optoelectronic devices. Functionalized nanocavity structures enhance the light–matter interaction and improve the light absorption in the ultrathin nanomembrane<sup>116</sup>. In general, most fast photodetectors have microsecond response speeds; very few devices can respond in nanoseconds. Ordered low-dimensional structures are an important route to pursue faster response speeds and meet the contemporary demand for high-speed electronic devices<sup>66</sup>.

## Integrated flexible UV systems

Wearable devices based on photodetectors track personal health the least invasively and are therefore very useful in the consumer market. The key problem to be solved is that conventional devices still lack overall flexibility and the ability to bend freely, owing to the rigid components (gate drivers and readout integrated circuits) of the flexible

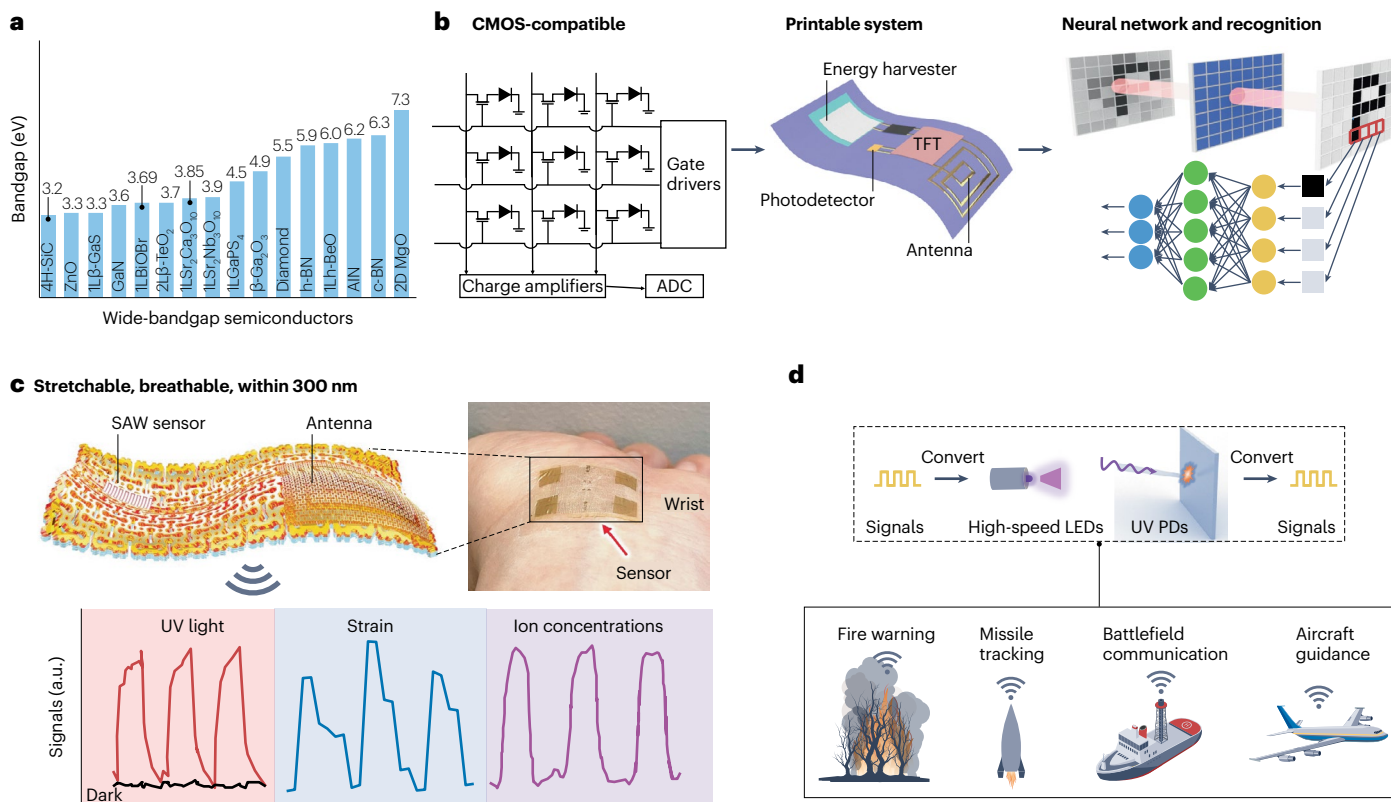


**Fig. 5 | Perspectives on UV photodetectors based on low-dimensional wide-bandgap semiconductors.** **a**, Typical wide-bandgap semiconductors and potential ultrawide bandgap semiconductors (bandgap higher than 6 eV), such as single-layer h-BeO, AlN, cubic boron nitride (c-BN) and 2D MgO. **b**, UV imaging technology is developing from complementary metal-oxide semiconductor (CMOS)-compatible to printable and flexible systems. State-of-the-art neuromorphic vision sensors can further enable intelligent imaging systems, which integrate sensing, memory and processing functions for integrated

flexible artificial visual systems<sup>121</sup>. **c**, A chip-less and wireless electronic skin based on a free-standing single-crystalline GaN ultrathin film. This device serves as a low-power-consumption health monitoring system to detect UV light, strain and ion concentrations in sweat with long-term stability<sup>97</sup>. **d**, Future scenarios for full UV communications, which are attractive for secure communication. ADC, analogue-to-digital converter; h-BN, hexagonal boron nitride; LED, light-emitting diode; PDs, photodetectors; SAW, surface acoustic wave; TFT, thin-film transistors. Panel c adapted with permission from ref. 97, AAAS.

imaging sensor. Fully integrated flexible UV systems can be constructed solely from flexible low-dimensional WBSs, which have the characteristics of stretchability, breathability, adaptability, high sensitivity, low power consumption and long-term wearability. A thin and flexible scanner, which will enable nail-to-nail fingerprint scanning in the future, is a promising step in the development of flexible UV imaging sensors<sup>117</sup>.

An important application prospect for WBS-based UV photodetectors is the integrated flexible UV system (Fig. 5b). Graphene charge-injection-based UV photodetectors provide an intriguing strategy to integrate this flexible UV imaging system, which includes non-destructive direct readout and IR photocharge injection from UV to mid-IR wavelengths. Additionally, an effective way to realize overall flexibility is to introduce wireless powered optoelectronic devices for sensing and processing signals, which includes printable elements (energy harvester, photodetector, antenna, capacitor, thin film transistor and so on). Furthermore, state-of-the-art neuromorphic vision sensors integrate sensing, memory and processing functions for an effective artificial visual system that possesses low power consumption and less redundant data in UV imaging applications<sup>118–120</sup>. This emerging in-sensor computing exhibits potential for flexible intelligent applications<sup>121</sup>. Although most reported neuromorphic sensors simulate the human visual system in the visible range<sup>122</sup>, UV sensing is also important for animal species (such as bees) to ensure their survival and reproduction. Inspired by this point, the development of the UV neuromorphic sensor could be attractive for flexible intelligent UV sensing devices<sup>119</sup>.

Rigid devices that lack a conformable interface with the skin cannot easily acquire accurate data of the human body. By contrast, the versatile health monitoring system shown in Fig. 5c, a chip-less wireless e-skin based on a free-standing single-crystalline GaN ultrathin film, detects UV light, strain and ion concentrations in sweat with long-term stability<sup>97</sup>. Graphene sensitized with semiconducting quantum dots promises a sensor structure without non-transparent and bulky readout electronics, benefitting from the intrinsic photoconductive gain<sup>123</sup>. Graphene quantum dots have also been used to build a broadband image sensor<sup>124</sup> and integrated with a flexible near field communication circuit board to fabricate a UV skin exposure monitoring system<sup>125</sup> that transfers data between photodetector and smartphone wirelessly and without batteries<sup>125</sup>. Without the obstacle of opaque and rigid readout circuitry, this monolithic monitoring system boasts enhanced transparency and flexibility while maintaining exceptionally high optoelectronic performance. Moreover, the development of scalable roll-to-roll production provides a mass-produced and low-cost pathway towards fully integrated wearable platforms.

## On-chip UV optical links

Optical communication technology has been widely studied from UV to IR light, and visible-range communication has realized a high data rate of more than 10 Gb s<sup>-1</sup> and a low bit-error rate of 3.8 × 10<sup>-3</sup> (ref. 126). With the rapid development of solar-blind photodetectors and deep-UV light-emitting diodes, UV communication has great potential to supplement traditional wireless communication, mainly owing to its advantages of low background noise, omnidirectional communication links and non-line-of-sight ability<sup>9</sup>. However, the photodetector and light source are still two main factors limiting applications in the era of the internet of things. It is believed that low-dimensional WBSs are promising candidates in UV communication systems, outperforming their conventional bulk counterparts, because they can realize high stability, high security, high speed, low power consumption and high integration. For example, the low-dimensional Ga<sub>2</sub>O<sub>3</sub> semiconductor, with its

bandgap of 4.9 eV, is highly suitable for solar-blind photodetectors. In particular, fabrication techniques are expected to improve in terms of material, device, manufacturing and encapsulation. Advanced printing techniques may be developed in the near future as scalable fabrication methods that enable effective integration with several optoelectronic elements, such as LEDs, microlenses and waveguides<sup>127</sup>. In this way, highly integrated and industrial-scale full UV communication systems are expected to be come true (Fig. 5d). More importantly, full optical link optoelectronic technology has greatly affected mobile devices and consumer electronics<sup>128,129</sup>. Controlled monolithic integration techniques need to be utilized to provide tight integration, higher bandwidth density and better efficiency. Low-dimensional semiconductor optoelectronics allow for releasing data traffic, improving integration density and reducing computing power consumption in the optical link process. Thus, low-dimensional WBSs demonstrate high UV absorption coefficients to serve as highly integrated high-speed photodetectors, which are important components of on-chip optical transceivers<sup>130</sup>.

In summary, from component design and preparation to dimensionality engineering, the morphologies and structures of WBSs can be directionally controlled, endowing them with intended properties. UV photodetectors based on low-dimensional WBSs can thus realize single or multifold practical functions or solve common problems faced in typical application scenarios. We hope this Review inspires more researchers to explore the complex properties of low-dimensional WBSs and to solve practical problems in the field of UV photodetectors.

Published online: 18 August 2023

## References

- Razeghi, M. & Rogalski, A. Semiconductor ultraviolet detectors. *J. Appl. Phys.* **79**, 7433–7473 (1996).
- Fortune, W. G., Scholz, M. S. & Fielding, H. H. UV photoelectron spectroscopy of aqueous solutions. *Acc. Chem. Res.* **55**, 3631–3640 (2022).
- Kneissl, M., Seong, T.-Y., Han, J. & Amano, H. The emergence and prospects of deep-ultraviolet light-emitting diode technologies. *Nat. Photonics* **13**, 233–244 (2019).
- Chen, H., Liu, K., Hu, L., Al-Ghamdi, A. A. & Fang, X. New concept ultraviolet photodetectors. *Mater. Today* **18**, 493–502 (2015).
- Zou, W., Sastry, M., Gooding, J. J., Ramanathan, R. & Bansal, V. Recent advances and a roadmap to wearable UV sensor technologies. *Adv. Mater. Technol.* **5**, 1901036 (2020).
- Araki, H. et al. Materials and device designs for an epidermal UV colorimetric dosimeter with near field communication capabilities. *Adv. Funct. Mater.* **27**, 1604465 (2017).
- Quyang, W., Chen, J., Shi, Z. & Fang, X. Self-powered UV photodetectors based on ZnO nanomaterials. *Appl. Phys. Rev.* **8**, 031315 (2021).
- García de Arquer, F. P., Armin, A., Meredith, P. & Sargent, E. H. Solution-processed semiconductors for next-generation photodetectors. *Nat. Rev. Mater.* **2**, 16100 (2017).
- Guo, L., Guo, Y., Wang, J. & Wei, T. Ultraviolet communication technique and its application. *J. Semicond.* **42**, 081801 (2021).
- Wang, X., Chen, Y., Liu, F. & Pan, Z. Solar-blind ultraviolet-C persistent luminescence phosphors. *Nat. Commun.* **11**, 2040 (2020).
- Cai, Q. et al. Progress on AlGaIn-based solar-blind ultraviolet photodetectors and focal plane arrays. *Light Sci. Appl.* **10**, 94 (2021).
- Jia, L., Zheng, W. & Huang, F. Vacuum-ultraviolet photodetectors. *Photonix* **1**, 22 (2020).
- Raeiszadeh, M. & Adeli, B. A critical review on ultraviolet disinfection systems against Covid-19 outbreak: applicability, validation, and safety considerations. *ACS Photonics* **7**, 2941–2951 (2020).
- Kneissl, M. & Rass, J. *III-Nitride Ultraviolet Emitters: Technology and Applications* Vol. 127 (Springer, 2015).
- Liu, M. et al. Colloidal quantum dot electronics. *Nat. Electron.* **4**, 548–558 (2021).
- Zhang, Q. et al. Enhanced gain and detectivity of unipolar barrier solar blind avalanche photodetector via lattice and band engineering. *Nat. Commun.* **14**, 418 (2023).
- Caldwell, J. D. et al. Photonics with hexagonal boron nitride. *Nat. Rev. Mater.* **4**, 552–567 (2019).
- Barrigón, E., Heurlin, M., Bi, Z., Monemar, B. & Samuelson, L. Synthesis and applications of III-V nanowires. *Chem. Rev.* **119**, 9170–9220 (2019).
- Ali, A. et al. in *2017 IEEE International Electron Devices Meeting (IEDM)* 8.6.1–8.6.4 (IEEE, 2017).
- Lev, L. L. et al. k-Space imaging of anisotropic 2D electron gas in GaN/GaAlN high-electron-mobility transistor heterostructures. *Nat. Commun.* **9**, 2653 (2018).
- Zhang, L., Dong, J. & Ding, F. Strategies, status, and challenges in wafer scale single crystalline two-dimensional materials synthesis. *Chem. Rev.* **121**, 6321–6372 (2021).



22. Quan, L. N., Kang, J., Ning, C.-Z. & Yang, P. Nanowires for photonics. *Chem. Rev.* **119**, 9153–9169 (2019).
23. Zheng, W., Huang, F., Zheng, R. & Wu, H. Low-dimensional structure vacuum-ultraviolet-sensitive ( $\lambda < 200$  nm) photodetector with fast-response speed based on high-quality AlN micro/nanowire. *Adv. Mater.* **27**, 3921–3927 (2015).
24. Romijn, J. et al. Integrated 64 pixel UV image sensor and readout in a silicon carbide CMOS technology. *Microsyst. Nanoeng.* **8**, 114 (2022).
25. Monroy, E., Omnès, F. & Calle, F. Wide-bandgap semiconductor ultraviolet photodetectors. *Semicond. Sci. Technol.* **18**, R33 (2003).
26. Gao, A. et al. Observation of ballistic avalanche phenomena in nanoscale vertical InSe/BP heterostructures. *Nat. Nanotechnol.* **14**, 217–222 (2019).
27. Yang, W. et al. 2D ultrawide bandgap semiconductors: odyssey and challenges. *Small Methods* **6**, 2101348 (2022).
28. Lee, J. S. et al. Wafer-scale single-crystal hexagonal boron nitride film via self-collimated grain formation. *Science* **362**, 817–821 (2018).
29. Ren, X. et al. Grain boundaries in chemical-vapor-deposited atomically thin hexagonal boron nitride. *Phys. Rev. Mater.* **3**, 014004 (2019).
30. Wang, L. et al. Epitaxial growth of a 100-square-centimetre single-crystal hexagonal boron nitride monolayer on copper. *Nature* **570**, 91–95 (2019).
31. Chen, T.-A. et al. Wafer-scale single-crystal hexagonal boron nitride monolayers on Cu(111). *Nature* **579**, 219–223 (2020).
32. Bets, K. V., Gupta, N. & Yakobson, I. How the complementarity at vicinal steps enables growth of 2D monocrystals. *Nano Lett.* **19**, 2027–2031 (2019).
33. Kim, Y. et al. Remote epitaxy through graphene enables two-dimensional material-based layer transfer. *Nature* **544**, 340–343 (2017).
34. Kim, H. et al. Remote epitaxy. *Nat. Rev. Methods Primers* **2**, 40 (2022).
35. Jeong, J. et al. Remote heteroepitaxy of GaN microrod heterostructures for deformable light-emitting diodes and wafer recycle. *Sci. Adv.* **6**, eaaz5180 (2020).
36. Jia, C., Lin, Z., Huang, Y. & Duan, X. Nanowire electronics: from nanoscale to macroscale. *Chem. Rev.* **119**, 9074–9135 (2019).
37. Huang, C.-T. et al. GaN nanowire arrays for high-output nanogenerators. *J. Am. Chem. Soc.* **132**, 4766–4771 (2010).
38. Kuykendall, T. R., Altoe, M. V. P., Ogletree, D. F. & Aloni, S. Catalyst-directed crystallographic orientation control of GaN nanowire growth. *Nano Lett.* **14**, 6767–6773 (2014).
39. Kuykendall, T. et al. Crystallographic alignment of high-density gallium nitride nanowire arrays. *Nat. Mater.* **3**, 524–528 (2004).
40. Fernández-Garrido, S., Zettler, J. K., Geelhaar, L. & Brandt, O. Monitoring the formation of nanowires by line-of-sight quadrupole mass spectrometry: a comprehensive description of the temporal evolution of GaN nanowire ensembles. *Nano Lett.* **15**, 1930–1937 (2015).
41. Fang, Z. et al. Si donor incorporation in GaN nanowires. *Nano Lett.* **15**, 6794–6801 (2015).
42. Bae, S.-Y. et al. Highly elongated vertical GaN nanorod arrays on Si substrates with an AlN seed layer by pulsed-mode metal–organic vapor deposition. *CrystEngComm* **18**, 1505–1514 (2016).
43. Ondry, J. C., Philbin, J. P., Lostica, M., Rabani, E. & Alivisatos, A. P. Colloidal synthesis path to 2D crystalline quantum dot superlattices. *ACS Nano* **15**, 2251–2262 (2021).
44. Balazs, D. M. et al. Electron mobility of  $24 \text{ cm}^2 \text{ V}^{-1} \text{ s}^{-1}$  in PbSe colloidal-quantum-dot superlattices. *Adv. Mater.* **30**, 1802265 (2018).
45. Pinna, J. et al. Approaching bulk mobility in PbSe colloidal quantum dots 3D superlattices. *Adv. Mater.* **35**, 2207364 (2023).
46. Coropceanu, I., Boles, M. A. & Talapin, D. V. Systematic mapping of binary nanocrystal superlattices: the role of topology in phase selection. *J. Am. Chem. Soc.* **141**, 5728–5740 (2019).
47. Nagaoka, Y., Zhu, H., Eggert, D. & Chen, O. Single-component quasicrystalline nanocrystal superlattices through flexible polygon tiling rule. *Science* **362**, 1396–1400 (2018).
48. Kaushik, S. et al. Deep-ultraviolet photodetectors based on hexagonal boron nitride nanosheets enhanced by localized surface plasmon resonance in Al nanoparticles. *ACS Appl. Nano Mater.* **5**, 7481–7491 (2022).
49. Veeralingam, S., Durai, L., Yadav, P. & Badhulika, S. Record-high responsivity and detectivity of a flexible deep-ultraviolet photodetector based on solid state-assisted synthesized hBN nanosheets. *ACS Appl. Electron. Mater.* **3**, 1162–1169 (2021).
50. Nasiri, N., Bo, R., Wang, F., Fu, L. & Tricoli, A. Ultraporous electron-depleted ZnO nanoparticle networks for highly sensitive portable visible-blind UV photodetectors. *Adv. Mater.* **27**, 4336–4343 (2015).
51. Jin, Y., Wang, J., Sun, B., Blakesley, J. C. & Greenham, N. C. Solution-processed ultraviolet photodetectors based on colloidal ZnO nanoparticles. *Nano Lett.* **8**, 1649–1653 (2008).
52. Tsai, D.-S. et al. Ultra-high-responsivity broadband detection of Si metal–semiconductor–metal Schottky photodetectors improved by ZnO nanorod arrays. *ACS Nano* **5**, 7748–7753 (2011).
53. Shi, L. & Nihtianov, S. Comparative study of silicon-based ultraviolet photodetectors. *IEEE Sens. J.* **12**, 2453–2459 (2012).
54. Saha, A. et al. Visible-blind ZnMgO colloidal quantum dot downconverters expand silicon CMOS sensors spectral coverage into ultraviolet and enable UV-band discrimination. *Adv. Mater.* **34**, 2109498 (2022).
55. Mitra, S. et al. High-performance solar-blind flexible deep-UV photodetectors based on quantum dots synthesized by femtosecond-laser ablation. *Nano Energy* **48**, 551–559 (2018).
56. Guo, F. et al. A nanocomposite ultraviolet photodetector based on interfacial trap-controlled charge injection. *Nat. Nanotechnol.* **7**, 798–802 (2012).
57. Ning, Y. et al. Spatially controlled occlusion of polymer-stabilized gold nanoparticles within ZnO. *Angew. Chem. Int. Ed.* **58**, 4302–4307 (2019).
58. Shao, D., Zhu, W., Xin, G., Lian, J. & Sawyer, S. Inorganic vacancy-ordered perovskite  $\text{Cs}_2\text{SnCl}_6/\text{Bi}/\text{GaN}$  heterojunction photodiode for narrowband, visible-blind UV detection. *Appl. Phys. Lett.* **115**, 121106 (2019).
59. Jin, Z. et al. Graphdiyne: ZnO nanocomposites for high-performance UV photodetectors. *Adv. Mater.* **28**, 3697–3702 (2016).
60. Liang, G., Mo, F., Ji, X. & Zhi, C. Non-metallic charge carriers for aqueous batteries. *Nat. Rev. Mater.* **6**, 109–123 (2021).
61. Yan, R., Gargas, D. & Yang, P. Nanowire photonics. *Nat. Photonics* **3**, 569–576 (2009).
62. Liu, X. et al. All-printable band-edge modulated ZnO nanowire photodetectors with ultra-high detectivity. *Nat. Commun.* **5**, 4007 (2014).
63. Cao, L. et al. Engineering light absorption in semiconductor nanowire devices. *Nat. Mater.* **8**, 643–647 (2009).
64. Krogstrup, P. et al. Single-nanowire solar cells beyond the Shockley–Queisser limit. *Nat. Photonics* **7**, 306–310 (2013).
65. Hu, L. & Chen, G. Analysis of optical absorption in silicon nanowire arrays for photovoltaic applications. *Nano Lett.* **7**, 3249–3252 (2007).
66. Cuesta, S. et al. Effect of bias on the response of GaN Axial p–n junction single-nanowire photodetectors. *Nano Lett.* **19**, 5506–5514 (2019).
67. Li, Y. et al. Efficient assembly of bridged  $\beta\text{-Ga}_2\text{O}_3$  nanowires for solar-blind photodetection. *Adv. Funct. Mater.* **20**, 3972–3978 (2010).
68. Xu, X. et al. A real-time wearable UV-radiation monitor based on a high-performance p–CuZnS/n–TiO<sub>2</sub> photodetector. *Adv. Mater.* **30**, 1803165 (2018).
69. Li, Q., Meng, J., Huang, J. & Li, Z. Plasmon-induced pyro-phototronic effect enhancement in self-powered UV–Vis detection with a ZnO/CuO p–n junction device. *Adv. Funct. Mater.* **32**, 2108903 (2022).
70. Liu, X. et al. Photovoltage-competing dynamics in photoelectrochemical devices: achieving self-powered spectrally distinctive photodetection. *Adv. Funct. Mater.* **32**, 2104515 (2022).
71. Wang, D. et al. Bidirectional photocurrent in p–n heterojunction nanowires. *Nat. Electron.* **4**, 645–652 (2021).
72. Deng, X., Li, Z., Cao, F., Hong, E. & Fang, X. Woven fibrous photodetectors for scalable UV optical communication device. *Adv. Funct. Mater.* **33**, 2213334 (2023).
73. Wang, S. et al. Two-dimensional devices and integration towards the silicon lines. *Nat. Mater.* **21**, 1225–1239 (2022).
74. Wang, S., Liu, X. & Zhou, P. The road for 2D semiconductors in the silicon age. *Adv. Mater.* **34**, 2106886 (2022).
75. Liu, Y., Huang, Y. & Duan, X. Van der Waals integration before and beyond two-dimensional materials. *Nature* **567**, 323–333 (2019).
76. Yang, F. et al. 2D organic materials for optoelectronic applications. *Adv. Mater.* **30**, 1702415 (2018).
77. Chen, W. et al. Giant five-photon absorption from multidimensional core–shell halide perovskite colloidal nanocrystals. *Nat. Commun.* **8**, 15198 (2017).
78. Roy, S. et al. Structure, properties and applications of two-dimensional hexagonal boron nitride. *Adv. Mater.* **33**, 2101589 (2021).
79. Li, J. et al. Dielectric strength, optical absorption, and deep ultraviolet detectors of hexagonal boron nitride epilayers. *Appl. Phys. Lett.* **101**, 171112 (2012).
80. Song, S.-B. et al. Deep-ultraviolet electroluminescence and photocurrent generation in graphene/hBN/graphene heterostructures. *Nat. Commun.* **12**, 7134 (2021).
81. Wang, F. et al. Liquid-alloy-assisted growth of 2D ternary  $\text{Ga}_2\text{In}_2\text{S}_3$  toward high-performance UV photodetection. *Adv. Mater.* **31**, 1806306 (2019).
82. Gong, C. et al. Large-scale ultrathin 2D wide-bandgap BiOBr nanoflakes for gate-controlled deep-ultraviolet phototransistors. *Adv. Mater.* **32**, 1908242 (2020).
83. Liu, X. et al. Boosted responsivity and tunable spectral response in B-site substituted 2D  $\text{Ca}_2\text{Nb}_{3-x}\text{Ta}_x\text{O}_{10}$  perovskite photodetectors. *Adv. Funct. Mater.* **31**, 2101480 (2021).
84. Wu, J. et al. Epitaxial growth of 2D ultrathin metastable  $\gamma\text{-Bi}_2\text{O}_3$  flakes for high performance ultraviolet photodetection. *Small* **18**, 2104244 (2022).
85. Al Balushi, Z. Y. et al. Two-dimensional gallium nitride realized via graphene encapsulation. *Nat. Mater.* **15**, 1166–1171 (2016).
86. Li, S., Zhang, Y., Yang, W., Liu, H. & Fang, X. 2D perovskite  $\text{Sr}_2\text{Nb}_3\text{O}_{10}$  for high-performance UV photodetectors. *Adv. Mater.* **32**, 1905443 (2020).
87. Liu, W. et al. Graphene charge-injection photodetectors. *Nat. Electron.* **5**, 281–288 (2022).
88. Zhang, Z. et al. All-in-one two-dimensional retinomorphic hardware device for motion detection and recognition. *Nat. Nanotechnol.* **17**, 27–32 (2022).
89. Wang, C.-Y. et al. Gate-tunable van der Waals heterostructure for reconfigurable neural network vision sensor. *Sci. Adv.* **6**, eaba6173 (2020).
90. Zhu, X. et al. Negative phototransistors with ultrahigh sensitivity and weak-light detection based on 1D/2D molecular crystal p–n heterojunctions and their application in light encoders. *Adv. Mater.* **34**, 2201364 (2022).
91. Fan, Z. et al. Electrical and photoconductive properties of vertical ZnO nanowires in high density arrays. *Appl. Phys. Lett.* **89**, 213110 (2006).
92. Chen, Y. et al. 3D solar-blind  $\text{Ga}_2\text{O}_3$  photodetector array realized via origami method. *Adv. Funct. Mater.* **29**, 1906040 (2019).
93. Li, X.-X. et al. High responsivity and flexible deep-UV phototransistor based on Ta-doped  $\beta\text{-Ga}_2\text{O}_3$ . *npj Flex. Electron.* **6**, 47 (2022).
94. Lien, D.-H. et al. 360° Omnidirectional, printable and transparent photodetectors for flexible optoelectronics. *npj Flex. Electron.* **2**, 19 (2018).



95. Liu, G. et al. Upconversion under photon trapping in ZnO/BN nanoarray: an ultrahigh responsivity solar-blind photodetecting paper. *Small* **18**, 2200563 (2022).
96. Fang, Z. et al. Pull-to-peel of two-dimensional materials for the simultaneous determination of elasticity and adhesion. *Nano Lett.* **23**, 742–749 (2023).
97. Kim, Y. et al. Chip-less wireless electronic skins by remote epitaxial freestanding compound semiconductors. *Science* **377**, 859–864 (2022).
98. Li, Z. et al. Mechanically compatible UV photodetectors based on electrospun free-standing  $Y^{3+}$ -doped  $TiO_2$  nanofibrous membranes with enhanced flexibility. *Adv. Funct. Mater.* **30**, 2005291 (2020).
99. Miyamoto, A. et al. Inflammation-free, gas-permeable, lightweight, stretchable on-skin electronics with nanomeshes. *Nat. Nanotechnol.* **12**, 907–913 (2017).
100. Chen, B. et al. Solar X-ray and EUV imager on board the FY-3E satellite. *Light Sci. Appl.* **11**, 329 (2022).
101. Zhang, Z. et al. In-sensor reservoir computing system for latent fingerprint recognition with deep ultraviolet photo-synapses and memristor array. *Nat. Commun.* **13**, 6590 (2022).
102. Gu, L. et al. A biomimetic eye with a hemispherical perovskite nanowire array retina. *Nature* **581**, 278–282 (2020).
103. Wu, W. et al. Ultrathin and conformable lead halide perovskite photodetector arrays for potential application in retina-like vision sensing. *Adv. Mater.* **33**, 2006006 (2021).
104. Cao, F., Yan, T., Li, Z., Wu, L. & Fang, X. Dual-band perovskite bulk heterojunction self-powered photodetector for encrypted communication and imaging. *Adv. Opt. Mater.* **10**, 2200786 (2022).
105. Bian, Y. et al. Spatially nanoconfined N-type polymer semiconductors for stretchable ultrasensitive X-ray detection. *Nat. Commun.* **13**, 7163 (2022).
106. Fountaine, K. T., Cheng, W.-H., Bukowsky, C. R. & Atwater, H. A. Near-unity unselective absorption in sparse InP nanowire arrays. *ACS Photonics* **3**, 1826–1832 (2016).
107. Gibson, S. J. et al. Tapered InP nanowire arrays for efficient broadband high-speed single-photon detection. *Nat. Nanotechnol.* **14**, 473–479 (2019).
108. Wang, D. et al. Observation of polarity-switchable photoconductivity in III-nitride/MoSe<sub>2</sub> core-shell nanowires. *Light Sci. Appl.* **11**, 227 (2022).
109. Hoang, C. V. et al. Interplay of hot electrons from localized and propagating plasmons. *Nat. Commun.* **8**, 771 (2017).
110. Hsu, A. L. et al. Graphene-based thermopile for thermal imaging applications. *Nano Lett.* **15**, 7211–7216 (2015).
111. Guo, J. X. et al. Infrared photodetectors for multidimensional optical information acquisition. *J. Infrared Millim. Waves* **41**, 40–60 (2022).
112. Zheng, Z. et al. Gallium nitride-based complementary logic integrated circuits. *Nat. Electron.* **4**, 595–603 (2021).
113. Zou, W. et al. Skin color-specific and spectrally-selective naked-eye dosimetry of UVA, B and C radiations. *Nat. Commun.* **9**, 3743 (2018).
114. Gao, N. et al. Quantum state engineering with ultra-short-period  $(AlN)_m/(GaN)_n$  superlattices for narrowband deep-ultraviolet detection. *Nanoscale* **6**, 14733–14739 (2014).
115. Gao, N. et al. Integral monolayer-scale featured digital-alloyed AlN/GaN superlattices using hierarchical growth units. *Cryst. Growth Des.* **19**, 1720–1727 (2019).
116. Xia, Z. et al. Single-crystalline germanium nanomembrane photodetectors on foreign nanocavities. *Sci. Adv.* **3**, e1602783 (2017).
117. van Breemen, A. J. J. M. et al. A thin and flexible scanner for fingerprints and documents based on metal halide perovskites. *Nat. Electron.* **4**, 818–826 (2021).
118. Shastri, B. J. et al. Photonics for artificial intelligence and neuromorphic computing. *Nat. Photonics* **15**, 102–114 (2021).
119. Li, G. et al. Photo-induced non-volatile  $VO_2$  phase transition for neuromorphic ultraviolet sensors. *Nat. Commun.* **13**, 1729 (2022).
120. Park, H.-L. et al. Retina-inspired carbon nitride-based photonic synapses for selective detection of UV light. *Adv. Mater.* **32**, 1906899 (2020).
121. Zhou, F. et al. Optoelectronic resistive random access memory for neuromorphic vision sensors. *Nat. Nanotechnol.* **14**, 776–782 (2019).
122. Li, Q., van de Groep, J., Wang, Y., Kik, P. G. & Brongersma, M. L. Transparent multispectral photodetectors mimicking the human visual system. *Nat. Commun.* **10**, 4982 (2019).
123. Konstantatos, G. et al. Hybrid graphene–quantum dot phototransistors with ultrahigh gain. *Nat. Nanotechnol.* **7**, 363–368 (2012).
124. Goossens, S. et al. Broadband image sensor array based on graphene–CMOS integration. *Nat. Photonics* **11**, 366–371 (2017).
125. Polat, E. O. et al. Flexible graphene photodetectors for wearable fitness monitoring. *Sci. Adv.* **5**, eaaw7846 (2019).
126. Rajbhandari, S. et al. A review of gallium nitride LEDs for multi-gigabit-per-second visible light data communications. *Semicond. Sci. Technol.* **32**, 023001 (2017).
127. Ren, A. et al. Emerging light-emitting diodes for next-generation data communications. *Nat. Electron.* **4**, 559–572 (2021).
128. Atabaki, A. H. et al. Integrating photonics with silicon nanoelectronics for the next generation of systems on a chip. *Nature* **556**, 349–354 (2018).
129. Mauthe, S. et al. High-speed III–V nanowire photodetector monolithically integrated on Si. *Nat. Commun.* **11**, 4565 (2020).
130. Kim, I. et al. Nanophotonics for light detection and ranging technology. *Nat. Nanotechnol.* **16**, 508–524 (2021).
131. Li, M.-Y. et al. Ultrahigh responsivity UV photodetector based on Cu Nanostructure/ZnO QD hybrid architectures. *Small* **15**, 1901606 (2019).
132. Liu, S. et al. Broad-band high-sensitivity ZnO colloidal quantum dots/self-assembled Au nanoantennas heterostructures photodetectors. *ACS Appl. Mater. Interfaces* **10**, 32516–32525 (2018).
133. Gong, M. et al. All-printable ZnO quantum dots/graphene van der Waals heterostructures for ultrasensitive detection of ultraviolet light. *ACS Nano* **11**, 4114–4123 (2017).
134. Luo, G. et al. High-performance ultraviolet photodetectors enabled by van der Waals Schottky junction based on  $TiO_2$  nanorod arrays/Au-modulated  $Ti_3C_2T_x$  MXene. *Adv. Funct. Mater.* **33**, 2211610 (2023).
135. Li, Y. et al. Solution-processed one-dimensional  $CsCu_2I_3$  nanowires for polarization-sensitive and flexible ultraviolet photodetectors. *Mater. Horiz.* **7**, 1613–1622 (2020).
136. Wang, D. et al. Highly uniform, self-assembled AlGaIn nanowires for self-powered solar-blind photodetector with fast-response speed and high responsivity. *Adv. Opt. Mater.* **9**, 2000893 (2021).
137. Xie, C. et al. Catalyst-free vapor–solid deposition growth of  $\beta$ - $Ca_2O_3$  nanowires for DUV photodetector and image sensor application. *Adv. Opt. Mater.* **7**, 1901257 (2019).
138. You, D. et al. Single-crystal ZnO/AlN core/shell nanowires for ultraviolet emission and dual-color ultraviolet photodetection. *Adv. Opt. Mater.* **7**, 1801522 (2019).
139. Park, T. et al. Aspect ratio-controlled ZnO nanorods for highly sensitive wireless ultraviolet sensor applications. *J. Mater. Chem. C* **5**, 12256–12263 (2017).
140. Zhang, Y. et al. High-performance two-dimensional perovskite  $Ca_2Nb_3O_{10}$  UV photodetectors. *Nano Lett.* **21**, 382–388 (2021).
141. Zhang, Y.-Y. et al. High performance flexible visible-blind ultraviolet photodetectors with two-dimensional electron gas based on unconventional release strategy. *ACS Nano* **15**, 8386–8396 (2021).
142. Yu, H. et al. Atomic-thin ZnO sheet for visible-blind ultraviolet photodetection. *Small* **16**, 2005520 (2020).
143. Han, W. et al. Atomically thin oxyhalide solar-blind photodetectors. *Small* **16**, 2000228 (2020).
144. Yan, Y. et al. Direct wide bandgap 2D GeSe<sub>2</sub> monolayer toward anisotropic UV photodetection. *Adv. Opt. Mater.* **7**, 1900622 (2019).
145. Liao, M. & Koide, Y. High-performance metal–semiconductor–metal deep-ultraviolet photodetectors based on homoepitaxial diamond thin film. *Appl. Phys. Lett.* **89**, 113509 (2006).
146. Furlan, F. et al. Tuning halide composition allows low dark current perovskite photodetectors with high specific detectivity. *Adv. Opt. Mater.* **10**, 2201816 (2022).
147. Fang, Y., Armin, A., Meredith, P. & Huang, J. Accurate characterization of next-generation thin-film photodetectors. *Nat. Photonics* **13**, 1–4 (2019).
148. Kublitski, J. et al. Reverse dark current in organic photodetectors and the major role of traps as source of noise. *Nat. Commun.* **12**, 551 (2021).
149. Han, S. et al. Anisotropic growth of centimeter-size  $CsCu_2I_3$  single crystals with ultra-low trap density for aspect-ratio-dependent photodetectors. *Adv. Sci.* **10**, 2206417 (2023).
150. Li, Z., Liu, X., Zuo, C., Yang, W. & Fang, X. Supersaturation-controlled growth of monolithically integrated lead-free perovskite single-crystalline thin film for high-sensitivity photodetectors. *Adv. Mater.* **33**, 2103010 (2021).
151. Yan, T., Cai, S., Hu, Z., Li, Z. & Fang, X. Ultrafast speed, dark current suppression, and self-powered enhancement in  $TiO_2$ -based ultraviolet photodetectors by organic layers and Ag nanowires regulation. *J. Phys. Chem. Lett.* **12**, 9912–9918 (2021).
152. Chen, J. et al. Work-function-tunable MXenes electrodes to optimize p-Cu<sub>2</sub>I<sub>2</sub>/n-Ca<sub>2</sub>Nb<sub>3</sub>O<sub>10</sub> junction photodetectors for image sensing and logic electronics. *Adv. Funct. Mater.* **32**, 2201066 (2022).

### Acknowledgements

The work was supported by the National Key R&D Program of China (No. 2022YFA1402904), National Natural Science Foundation of China (Nos 62204047, 92263106, 12061131009 and 1221530438) and the Science and Technology Commission of Shanghai Municipality (No. 21520712600 and 19520744300).

### Author contributions

Z.L. and T.Y. contributed equally to this work. X.F. supervised the manuscript. All authors contributed to the discussion of content, writing and editing of the manuscript before submission.

### Competing interests

The authors declare no competing interests.

### Additional information

**Peer review information** *Nature Reviews Materials* thanks Zhiyong Fan, Xiaohang Li and Lin-Bao Luo for their contribution to the peer review of this work.

**Publisher's note** Springer Nature remains neutral with regard to jurisdictional claims in published maps and institutional affiliations.

Springer Nature or its licensor (e.g. a society or other partner) holds exclusive rights to this article under a publishing agreement with the author(s) or other rightsholder(s); author self-archiving of the accepted manuscript version of this article is solely governed by the terms of such publishing agreement and applicable law.

© Springer Nature Limited 2023